Universidade de Aveiro
2018
Departamento de Engenharia de Materiais e Cerâmica

Rute Alexandra Correia Pereira

Desenvolvimento de nanopartículas magnéticas para dispositivos biomédicos

Development of magnetic nanoparticles for biomedical devices

Universidade de Aveiro
2018
Departamento de Engenharia de Materiais e Cerâmica

Rute Alexandra Correia Pereira

Desenvolvimento de nanopartículas magnéticas para dispositivos biomédicos

Development of magnetic nanoparticles for biomedical devices

Dissertação apresentada à Universidade de Aveiro para cumprimento dos requisitos necessários à obtenção do grau de Mestre em Materiais e Dispositivos Biomédicos, realizada sob orientação científica do Doutor Nuno João de Oliveira e Silva, Investigador Principal do Departamento de Física da Universidade de Aveiro.

Trabalho financiado pela Bolsa de Investigação BI/IU89/7529/2016 e enquadrado nos projetos CoolPoint P2020-PTDC-CTM-NAN-4511-2014 e CICECO-Aveiro Institute of Materials, POCI-01-0145-FEDER-007679 (FCT Ref. UID /CTM /50011/2013), financiados por fundos nacionais pela FCT/MEC e cofinanciado pelo FEDER sob acordo de parceria PT2020.

Para a minha família, que acaba de receber o seu novo membro.

Bem vindo ao mundo, João.

o júri

Presidente	**Doutor José Maria da Fonte Ferreira** Professor Associado com Agregação do Departamento de Engenharia de Materiais e Cerâmica da Universidade de Aveiro
Orientador	**Doutor Nuno João de Oliveira e Silva** Investigador Principal do Departamento de Física da Universidade de Aveiro
Arguente	**Doutor Vítor Brás Sequeira Amaral** Professor Catedrático do Departamento de Física da Universidade de Aveiro

agradecimentos

Nunca poderia deixar de relembrar todos os professores que foram os pilares da minha educação enquanto cientista. Nem poderia deixar de destacar o Professor que confiou nas minhas capacidades antes de qualquer outra pessoa. Obrigada Professor Fernando Domingues, espero que um dia nos voltemos a encontrar.

Doutora Filipa Sousa e Doutor Nuno João Silva, agradeço por todas as oportunidades que me proporcionaram até agora, e por acreditarem sempre em mim e nas minhas capacidades.

Ao Rui Silva, que me ensinou e continua a ensinar tudo o que sabe, e que mesmo longe só se encontra a uma chamada de distância.

Ao Doutor Vítor Gaspar e ao Professor João Mano estou grata por me terem aberto as portas dos seus laboratórios, e por toda a colaboração e aprendizagem que daí resultou.

Uma palavra de gratidão ao Pedro Nunes à Doutora Isabel Lopes por terem aceitado este desafio.

À Doutora Rosário Soares agradeço por toda a formação e ajuda que disponibilizou no âmbito da Difração de Raios X e pela amizade que entretanto se formou.

Agradeço aos meus colegas de laboratório, que promovem todos os dias o melhor ambiente de trabalho possível.

À minha família, a gratidão por me continuarem a apoiar nesta constante batalha pelo conhecimento, e pela compreensão durante todos os dias em que estamos afastados.

À minha melhor amiga de infância, Jéssica Ferreira, que sempre acompanhou, mesmo de longe, esta aventura. Obrigada por tudo.

Ao Tomás, agradeço pela presença constante, nos dias bons, nos menos bons e nas horas infindáveis de escrita, lado a lado.

palavras-chave

Nanopartículas Magnéticas, Hipertermia, Controlo de Temperatura, Imagiologia por Ressonância Magnética, Agentes de Contraste

resumo

Nas últimas décadas, as nanopartículas magnéticas têm vindo a ser desenvolvidas para aplicações biomédicas, tais como tratamento médico e imagiologia.

Em relação ao tratamento médico, as nanopartículas magnéticas têm sido extensivamente utilizadas em hipertermia, um tratamento que requere o aquecimento de células cancerígenas mas que não possui controlo de temperatura local, o que habitualmente provoca danos em células saudáveis. Esta tese aborda este problema utilizando nanopartículas de Fe_3Se_4 cuja temperatura de Curie se encontra ligeiramente acima de 40 ℃.

No que toca à imagiologia médica, nas últimas décadas têm vindo a ser desenvolvidas novas maneiras que permitam a manipulação do contraste. Nos dias de hoje, a utilização de agentes de contraste é comum quando se realiza uma Ressonância Magnética (MRI). Estes agentes de contraste podem ser moléculas, nanopartículas ou compostos, que alteram o ambiente magnético e podem depois aumentar ou diminuir o contraste da imagem obtida. As nanopartículas de Fe_3Se_4 aqui apresentadas são também avaliadas como agentes de contraste para MRI. Para além disto, o desenvolvimento de agentes de contraste de modo duplo representa uma nova geração, que tira vantagem dos dois modos de relaxação, permitindo um maior contraste entre tecidos doentes e saudáveis. Neste sentido, a presente tese também reporta o desenvolvimento de um novo método de síntese que dá origem a agentes de contraste de modo duplo que combinam nanopartículas de Fe_3O_4 e complexos organometálicos de Gadolínio.

As sínteses e caracterizações de todas as nanopartículas e complexos de Gadolínio são apresentadas, bem como avaliações ecotoxicológicas e citotóxicas das nanopartículas.

keywords

Magnetic Nanoparticles, Hyperthermia, Temperature Control, Magnetic Resonance Imaging, Contrast Agents

abstract

In the last decades, magnetic nanoparticles have been developed for biomedical applications, such as medical treatment and imaging.
In medical treatment, magnetic nanoparticles have been extensively used in hyperthermia, a treatment that requires the heating of cancer cells but lacks local temperature control, which often leads to damage in healthy cells. This thesis addresses this problem using Fe_3Se_4 nanoparticles that have a Curie temperature slightly above 40 ℃.
In medical imaging, the quest for contrast manipulation has been pursued during the last decades. The use of contrast agents is nowadays common when performing an MRI. These contrast agents are molecules, nanoparticles or compounds, that alter the magnetic environment and can later increase or decrease the contrast of the obtained image. Fe_3Se_4 nanoparticles here presented are also evaluated as contrast agents for MRI. In addition, the development of dual-mode contrast agents represents a new generation, which takes advantage of the two relaxation modes, allowing a higher contrast between healthy and unhealthy tissues. Regarding this, the present thesis also reports the development of a new synthesis approach to yield a dual-mode contrast agent that combines Fe_3O_4 nanoparticles and a Gadolinium based metal-organic complex.
Synthesis and characterizations of all the nanoparticles and Gadolinium complexes are presented, as well as the ecotoxicological and cytotoxic evaluations of the nanoparticles.

Contents

List of Figures

List of Tables

List of abbreviations

DDT	1-Dodecanethiol
DTPA	Diethylenetriaminepentaacetic acid
FC	Field Cool
HCG	Human Chorionic Gonadotropin
LED	Light-emitting diode
MRI	Magnetic Resonance Imaging
NIR	Near Infrared
NMR	Nuclear Magnetic Resonance
SR-latch	Set/reset flip-flop logic gate
TDPA	Tetradecylphosphonic acid
TEM	Transmission Electron Microscopy
XRD	X-ray Diffraction
ZFC	Zero Field Cool

List of symbols

μ_B	Bohr magneton
$\mathbf{B}_0$	Magnetic Field
$\mathbf{g}$	Landé g-factor
$\mathbf{h}$	Planck's constant
$\mathbf{k}_B$	Boltzmann constant
$\mathbf{M}_r$	Remanent Magnetization
s	Spin quantum number
$\mathbf{T}$	Temperature
$\mathbf{T}_1$	Spin-lattice relaxation time
$\mathbf{T}_2$	Spin-spin relaxation time
$\mathbf{T}_c$	Curie Temperature
γ	Gyromagnetic ratio
ν	Stretching vibration
τ_C	Correlation time
χ	Magnetic susceptibility
ω	Frequency
ω_0	Larmor frequency

1. Introduction

This Chapter starts by presenting the concepts of nanoparticles and nanomaterials. Secondly, nanoparticles are presented, as well as some of its applications, namely: (1) nanoparticles used as Logic Gates, (2) nanoparticles used as heat sources in hyperthermia and (3) nanoparticles used as contrast agents for Magnetic Resonance Imaging (MRI). Some theoretical concepts regarding these applications will also be presented.

1.1 What is a nanomaterial?

Nanomaterials are objects which have, at least, one dimension within the nanoscale. This scale conventionally ranges from one to a few hundred nanometers. A scale of sizes to enlighten the different orders of magnitude between a millimeter-sized object and a nanometer-sized object is presented in Figure 1 [1]. According to its origin, these nanomaterials can be divided in two classes. One corresponds to nano-objects that appear among nature, for example proteins, viruses, bacteria, nanoparticles produced during volcanic eruptions or during forest fires, nanostructured crystals and minerals, among others. The other includes nano-objects made by humans: nanoparticles produced from diesel or petrol combustion, power stations, and incinerators, and, also, nano-objects produced through a defined manufacturing process, intentionally [2].

Nanomaterials can also be categorized according to their dimensions: nanoparticles, with all three dimensions smaller than a few hundred nanometres [3]; nanowires or nanotubes, with two dimensions within the nanoscale [4]; and nanofilms or nanolayers, comprehending just one dimension within the nanometer range [5]. Depending on the applications, nanomaterials can be made of different elements or compounds: metals, such as gold or silver nanoparticles [6], metal oxides, such as titanium dioxide or iron oxide nanoparticles [3], and semiconductors, such as silicon or carbon, for example [2].

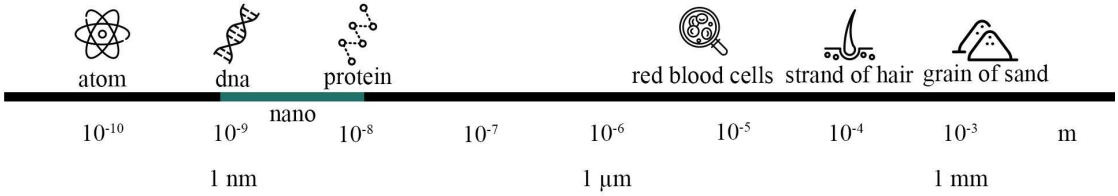

Figure 1 – Scale of sizes from an atom to a grain of sand to enlighten the nanoscale.

1.2 What changes at the nanoscale?

The major differences between nanomaterials and bulk sized materials are related to surface and size dependent effects [7]. At the nanoscale, nanomaterials can exhibit finite size effects, such as quantum confinement, which appears, for instance, in quantum dots, and superparamagnetism, which appears in small iron oxide nanoparticles [8]. Concerning the surface, as the radius of an object gets smaller, its surface/volume ratio increases, which allows more molecules to be anchored onto the surface, for example [1]. The surface geometry, the presence of surfactant or coating are parameters that substantially change the nanoparticle properties [9].

1.3 Nanoparticles

Nanoparticles can be classified according to its composition into either organic - including carbon nanotubes, liposomes, and fullerenes - or inorganic, including quatum dots and magnetic nanoparticles [10]. Nowadays scientists can produce nanoparticles with several shapes and sizes, depending on the desired applications. Nanoparticles can be found in different morphologies such as triangular gold nanoparticles [6], hexagonal boron nitride nanoparticles [11], spherical [12–14] and cubic [14–17] magnetite nanoparticles, amongst others [18,19]. There are also specific arrangements of different materials: core-shell, janus, dumbbell, half raspberry, acorn, and snowman, to name a few. In these cases, the nanoparticle has two or more different regions made of different compounds or materials [12, 20, 21].

Nanoparticles can be produced following two general approaches: by making the materials smaller, i.e., downscaling, and by constructing nanoparticles from small building blocks, i.e., upscaling. These two are referred as "top-down" and "bottom-up" approaches, respectively [22]. In general, there are three different methods for the synthesis of nanomaterials: chemical, physical and biological. Some chemical methods

include thermal decomposition, coprecipitation, sonochemical, electrochemical decomposition, hydrothermal and microemulsion [23, 24]. Examples of physical methods include aerosol, gas phase deposition, electron beam lithography, laser-induced pyrolysis, pulsed laser ablation and power ball milling [25]. Some biological methods are mediated by plants, fungi bacteria and proteins [26].

1.4 Applications of nanoparticles

The use of nanoparticles is known to be promising in several fields: electronics, catalysis, photocatalysis [27, 28], optics, materials science, engineering, biology and medicine [29], due to the peculiar properties of matter at nanoscale when compared to the properties of similar materials in the bulk form. In biology and medicine, the interplay between nanomaterials and biological systems forms an emerging research field: nanomedicine [4]. In fact, several nanoparticles have been prepared for diagnose and treatment, being integrated, for example, in sensors for biological molecules, hyperthermia or photothermal therapy [1, 2].

Magnetic nanoparticles, among the most commonly used ones, are inorganic and zero-dimensional materials usually with a transition metal ion-based composition (from the d and f groups of the periodic table) [1]. In addition to their magnetic properties, these nanoparticles exhibit biocompatibility and low toxicity, which makes them attractive for biomedical applications [30]. Biomedical applications that use magnetic nanoparticles are generally classified into *in vitro* (outside the body) and *in vivo* (inside the body). *In vitro* applications are mainly used in diagnostic processes, such as magnetic separation and magnetic sensing. *In vivo* applications include diagnostic processes, such as MRI, as well as therapeutic applications, for example drug delivery and magnetic hyperthermia [10].

1.4.1 Logic gates

A logic gate is a physical device that implements a Boolean function, i.e., a device that performs a logical operation on one or more binary inputs and produces a single binary output. The last years of research have brought molecules [31, 32] and smart nanomaterials capable of behaving as logic gates [33–35]. These materials are especially promising for the design of biosensors [36]. Typically, a biosensor has three fundamental elements: an input, a recognition mechanism and an output. Distinguishing himself from a common biosensor, a logical gate-based biosensor includes the possibility of multiple concurrently inputs, a rather complex biochemical

reaction to process these inputs (with the built-in Boolean logic), and a digital output, which is generally presented in a "YES/NO" format [37].

There are three basic logic gates: OR Gate, AND Gate and NOT Gate [38]. In an OR gate the output will be high (1) if either one or both inputs are high. The output will the low (0) only if both inputs are low. In an AND gate the output will be high only if both inputs are high. If any of the inputs is low then the output will be low. The NOT gate is known as an invertor. In this gate, the output will only be high if the input is low and vice-versa [39]. Another commonly used gate is the NOR gate. The NOR gate is a combination of an OR gate and a NOT gate connected in series. The inclusive NOR gate has an output that is normally high and is only low when any of its inputs are high. The NOR gate is the reverse form of the OR gate explained before [39].

Different types of gates can be combined in various configurations to construct devices based on sequential logic. In sequential logic, the output depends not only on the input signal, but also on the sequence of events. One example of a sequential logic-based device is the set/reset flip-flop logic gate (SR-latch), explained below [39].

SR-latch

A SR-latch is the simplest bi-stable device working as a memory element, which can be created by wiring two NOR gates in such way that the output of one feeds back to the input of another, and vice versa, as shown in Figure 2. The set and reset inputs, which place this memory element into a high or a low state, are labelled S and R respectively, and the complementary outputs Q and $\bar{Q}$ respectively [39].

A truth table of a SR-latch, Table 1, shows the output at a time t ($Q(t)$), the subsequent action on S, R, or both and the resulting output at a time t+1 ($Q(t+1)$). RC stands for "race condition", where the state $Q(t+1)$ is ill-defined and depends on which S or R is set low in first place.

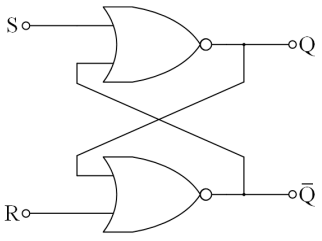

Figure 2 – A symbolic representation of a SR-latch.

Table 1 – Truth table of a SR-latch

$Q(t)$	S	R	$Q(t+1)$
0	0	0	0
0	0	1	0
0	1	0	1
0	1	1	RC
1	1	1	RC
1	0	0	1
1	0	1	0
1	1	0	1

1.4.2 Hyperthermia

Nowadays, hyperthermia is amongst the most studied therapeutic methods for cancer treatments, such as: breast, cervical, lung, head and neck, central nervous system, gastrointestinal, genitourinary, paediatric cancers, sarcoma and melanoma [40]. The term hyperthermia derives from two Greek words "hyper" and "therme", meaning "rise" and "heat", respectively. Relying on the vulnerability of cancer cells to heating, this treatment exposes the body tissue to high temperatures (between 39 and 45 °C), using an external energy source. In fact, *in vivo* studies have shown that temperatures in the range of 40-44 °C cause more selective damage to tumour cells [10, 40]. Although this technique has gained prospects and significant advances, it may also cause several discouragements and frustration because of undesirable effects, such as blisters, burns and pain, increasing rapidly in healthy cells [10].

Hyperthermia is divided three major categories: local, regional and whole-body. Local hyperthermia is generally used for localized diseased tissues near the surface of the skin or natural body orifices. Regional hyperthermia is generally used for deeper diseased tissues or when a larger area of treatment is required, for example, in the case of a locally advanced disease. Regional hyperthermia is achieved by increased perfusion of organs or limbs through blood heating, by irrigation of body cavities or through other non-invasive methods such as radiofrequency. Whole body hyperthermia is typically used to treat metastatic disease. The most common approach to whole body hyperthermia is the use of a flexible infrared chamber. Other methods may involve simply heating a patient's room or wrapping the patient in heated blankets. In addition to these simple ambient methods of inducing hyperthermia, more complex techniques have been developed that use infrared, RF, microwave and ultrasound [41, 42].

Nanoparticles can be used as heating sources in hyperthermia, based on different

principles. For example, gold nanoparticles can absorb and scatter incident light and convert resonant energy to heat, due to its surface plasmon resonance. Other examples include superparamagnetic nanoparticles that release heat when an alternated magnetic field is applied [43]. Nanoparticle-mediated hyperthermia is promising in poorly accessible and deep-seated tumours. With specific coatings, the nanoparticles are not recognized as invasors by the immune system and thus reach their targets [41]. The hyperthermia method has not been very effective to cure serious cancers because of basic problems associated with local hyperthermia. These problems include heterogeneous temperature distribution in tumour mass and incapability to prevent overheating at the deep-seated tumour region [10]. Arguably, the greater challenge has been the development of methods to detect the temperatures induced and maintained during the hyperthermia treatment. Thus, the idea of combining nanoparticles that can both heat the cells and also somehow indicate the temperature range appeared [44]. This idea and its development will be explored in this thesis.

1.4.3 Magnetic Resonance Imaging

Magnetic Resonance Imaging is the last application of the Nuclear Magnetic Resonance (NMR) technique, which is considered a powerful tool in many research fields: in chemical and pharmaceutical analysis for the investigation of molecular structure and molecular motion in solids and liquids, in solid state physics to study physical properties at the atomic level, in biomedicine to obtain information about organs, cells and tissues [45, 46]. In fact, nowadays, MRI has become one of the most important techniques in the diagnosis of many diseases, is considered a non-invasive powerful diagnostic method in medical science, which has shown several advantages, such as extreme imaging flexibility, non-ionizing, patient harmlessness, high patient acceptance, high-resolution images with an excellent soft tissue contrast between different tissues, prevision of physiological parameters, and acquisition of unique clinical information [47]. Particularly, it should be noted that for some pathologies MRI reached the highest resolution in images and the fastest acquisition times when compared to other imaging techniques [48].

How MRI works

MRI is an imaging technique based on the magnetic properties of the nuclei, which is excited by non-invasive radiofrequency (RF) radiation. The nuclei of some elements, such as Hydrogen, ^{1}H, have a fundamental angular momentum called spin, which causes them to behave as tiny spinning magnets, as shown in Figure 3 (a) [47]. When these

nuclei are placed in an uniform external magnetic field and excited by a radio pulse tuned to the Larmor frequency, the axis of rotation of the nuclei will precess around the applied magnetic field direction, as shown in Figure 3 (b). The Larmor frequency, w_0, is proportional to the externally applied magnetic field strength, B_0, through the expression $w_0 = \gamma B_0$, where γ is the gyromagnetic ratio [48].

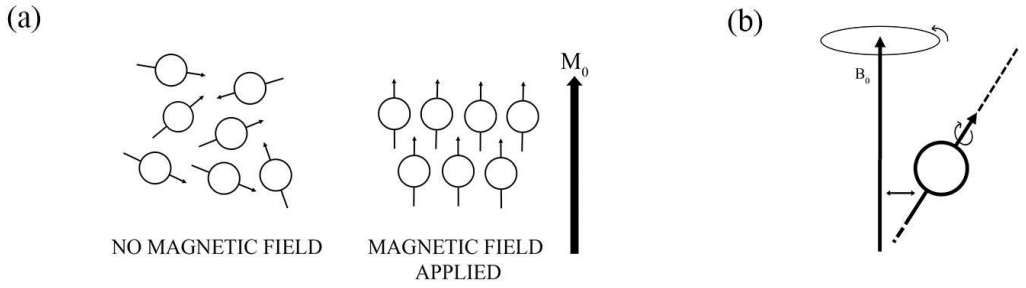

Figure 3 – **(a)** Behaviour of nuclear spin when in absence or in presence of a magnetic field; **(b)** Precession movement of the nuclear spin I around the magnetic field B_0.

The NMR experiment is based on the precession of a nuclear spin when immersed in a static magnetic field. Under this field, the degenerated energy levels become separated, giving origin to $2s+1$ energy levels, whereas s is the total spin quantum number. This effect is known as the Zeeman effect [48]. As shown in Figure 4, in a magnetic field, spinning nuclei have lower energy when aligned to the magnetic direction than when they are opposed to it. Simplifying, it can be considered only the nuclear spin of the hydrogen nucleus, ^{1}H, which is the most relevant one for MRI. The hydrogen nucleus has s=1/2, which gives rise to 2 non-degenerated energy levels, E_1 and E_2. This energy gap is given by $\Delta E = \gamma B_0$ and corresponds to a certain frequency ($v = \Delta E/h$) which is in the range of radio frequencies [48]. Thus, an RF pulse can change the relative populations between E_1 and E_2. After a stimulation by a RF pulse, the atomic nuclei population returns to an equilibrium state, through a process of relaxation. This relaxation process is described mainly by two microscopic time constants: the longitudinal one, T_1, called nuclear spin-lattice relaxation time and the transversal one, T_2, called nuclear spin-spin relaxation time. T_1 and T_2 are material-dependent, thus giving the possibility of distinguishing different tissues/diseases with a proper analysis of the received signal [48].

The interaction between the magnetic moments of the excited spins and the environment creates fluctuating local microscopic magnetic fields. These magnetic fluctuations are linked to the molecular movement [48]. Longitudinal, T_1, and transverse, T_2, relaxation times are therefore modulated by the phenomenon of molecular distribution and are

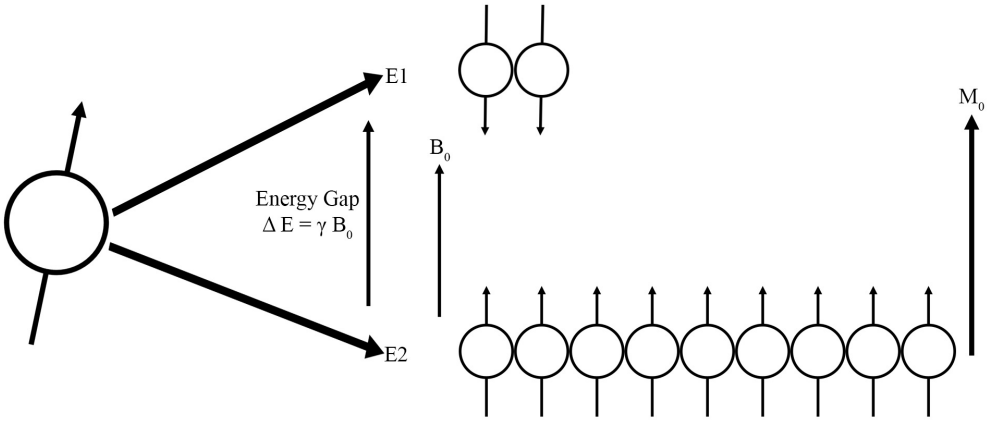

Figure 4 – Energy difference between spins when aligned to the magnetic field, B_0, and opposed to it.

expressed by the generic relationship:

$$1/T_i = R_i = KE_c^2 f(\tau_c) \tag{1.1}$$

where:

$i = 1, 2$

R_i is the relaxation rate,

K is a constant,

E_c is the amplitude of the interaction responsible for the relaxation,

$f(\tau_c)$ is a function of the correlation time, τ_c, that modulates the interaction.

Although the precession movement around the applied magnetic field does not provide imaging information, if the external magnetic field is made nonuniform in space, i.e. if a magnetic field gradient is utilized, then protons at different locations will precess at different frequencies, thereby creating a relationship between location in the body and precessional frequency. This method of imaging allows one to map the density of protons in the body in three dimensions, however, most images are obtained and displayed as planar cross-sectional images similar to those in Computer Tomography scans [45].

Contrast agents

The signal intensity of MRI depends not only on the proton density, but also on T_1 and T_2. Instrumental parameters such as the choice of sequence can also influence the contrast. Fortunately, T_1 and T_2 can be modulated by contrast agents. Contrast agents have to be stable, non toxic, biocompatible and must present efficiency and safety for the patient before being considered for medical application. The efficiency of contrast agents relies on their relaxivity, defined as the aptitude to increase the water proton relaxation rate [48, 49].

The two major categories of contrast agents are paramagnetic and superparamagnetic. Paramagnetic compounds typically affect T_1 (positive contrast agents, which exhibit "bright" contrast) and superparamagnetic compounds affect T_2 (negative contrast agents, which exhibit "dark" contrast). Positive contrast agents reduce the R_2/R_1 ratio by reducing T_1 while negative contrast agents increase the R_2/R_1 ratio by reducing T_2. Paramagnetic agents are usually composed of a metal ion which has a permanent magnetic moment due to unpaired electrons, for example Gadolinium, Gd^{3+}, and a chelating ligand, such as diethylenetriaminepentaacetic acid, DTPA. The magnetization of paramagnetic materials, such as Gadolinium complexes, is directly dependent on the ion unpaired electrons and the number of ions, having no magnetization in the absence of an external magnetic field. There are several transition metals and lanthanide metals with unpaired spins, but for the metal to be effective as a relaxation agent the electron spin-relaxation time must match the Larmor frequency of the protons. This condition is better met for the Fe^{3+} and Gd^{3+} ions [47]. The most common superparamagnetic agents are made of an iron oxide core covered in a polymer matrix to prevent aggregation. Superparamagnetic agents form a significantly larger magnetic moment than the paramagnetic agents.

A new generation of contrast agents comprises the combination of paramagnetic and superparamagnetic centres, to achieve a situation where both T_1 and T_2 can be actuated. Some materials have been developed for this purpose, including combinations in different constitutions of Gd^{3+} and iron oxide nanoparticles. Some examples are Gd-doped superparamagnetic iron oxide nanoparticles [50], core-shell nanoparticles [51, 52], or microspheres [53]. Yet, the combinations of the two magnetic centres tend to be performed in several steps, which implies more reactions, resources, and time.

1.5 Aim of the thesis

The aim of the thesis is to develop two types of nanoparticles, namely Fe_3Se_4 and Fe_3O_4 nanoparticles, for two different biomedical applications. Fe_3Se_4 nanoparticles will be used as a logic gate for the determination of whether or not a temperature threshold was exceeded during hyperthermia treatment *in vitro*, where Prostate Cancer cells are heated with a Near Infrared (NIR) LED. Fe_3Se_4 nanoparticles will also be evaluated as contrast agents for MRI, and Fe_3O_4 nanoparticles will be functionalized with Gadolinium complexes in order to achieve a dual-mode contrast agent for MRI. The cytotoxicity of these nanoparticles will be evaluated in Prostate Cancer Cells as well as its ecotoxycological effect on *Xenopus laevis*, an amphibian model organism.

2. Synthesis and Characterization

This Chapter presents the state of the art of synthesis of Fe_3O_4 and Fe_3Se_4 nanoparticles, and describes the selected procedures for this thesis, as well as all the characterization techniques used to analyse the prepared nanomaterials. It is also presented the innovative one step phase exchange and functionalization procedure that allows nanoparticles to be coated with small catechol-based biomolecules.

2.1 Fe_3O_4 nanoparticles

Iron oxides are usually found in nature and can be easily synthesized in the laboratory [54]. During the last decade, the synthetic routes for the preparation of iron oxide nanoparticles have been intensively developed due to its fundamental scientific interest and its many technological applications [55]. Among these, some of the most interesting applications have been drug delivery, MRI, magnetic hyperthermia, thermoablation, bioseparation and biosensing [56, 57]. Bioapplications based on magnetic nanoparticles have been receiving considerable attention due to the unique advantages nanoparticles present when compared to other materials. Some of these advantages include the ability to produce iron oxide nanoparticles with a small economic budget, yielding physically and chemically stable, biocompatible, and environmentally safe nanoparticles [58, 59].

Magnetite (Fe_3O_4) and maghemite (γ-Fe_2O_3) are two examples of ferrimagnetic iron oxides that are widely used in several applications. Magnetite has tetrahedral cation sites occupied by Fe^{3+} ions and octahedral cation sites occupied by Fe^{3+} and Fe^{2+} ions. The magnetic moments of Fe^{3+} and Fe^{2+} have different magnitudes. This means that even when the spins are placed in an antiparallel arrangement, the net magnetic moment is different than zero - such arrangement occurs below the Curie temperature (approximately 850 K). This antiparallel unbalanced arrangement is called ferrimagnetism. On the other hand, maghemite is ferrimagnetic due to another reason. Similarly to magnetite, maghemite has two sublattices corresponding to Fe^{3+} ions

located on tetrahedral and octahedral sites. The atomic moments within each sublattice are parallel, although, the two sublattices are unequal in number and arranged in an antiparallel form, leading to a non zero net magnetization, again in a ferrimagnetic fashion [60]. Ferrimagnetic iron oxide nanoparticles can be synthesized through a variety of synthetic methods. Some examples include coprecipitation, thermal decomposition, hydrothermal and solvothermal synthesis, sol-gel synthesis, microemulsion, ultrasound irradiation and biological synthesis [22]. Conventionally, these methods can be divided into aqueous and non-aqueous routes. Aqueous approaches are commonly used due to their low cost and sustainability. As the most used aqueous approach, the coprecipitation method consists of mixing iron salts in very basic solutions at room temperature or at medium temperature ($\leq$ 100°C), under an inert atmosphere (usually Nitrogen) [23]. However, in this method, control over particle size, morphology and composition is limited [22]. Regarding this, different alternative strategies have been developed such as nonaqueous thermal decomposition methods [14]. A typical difference between a coprecipitation synthesis and a thermal decomposition synthesis can be observed in Figure 5.

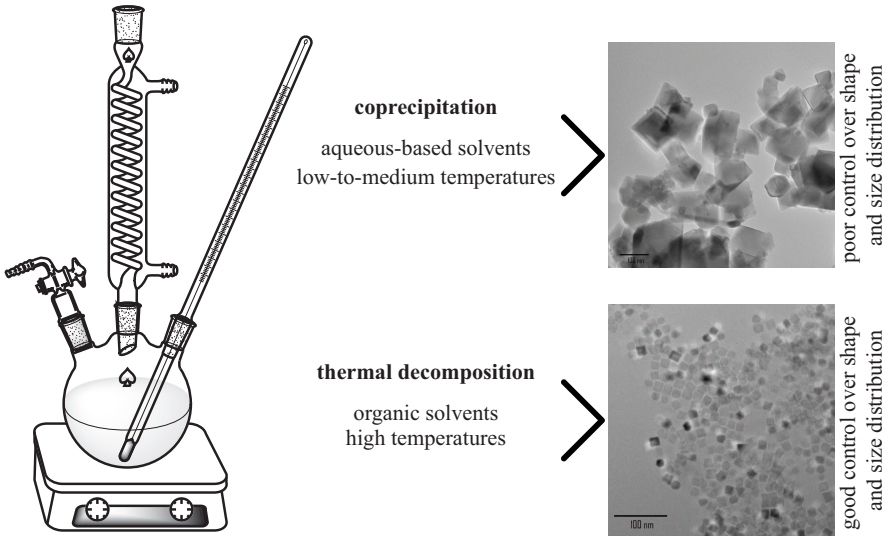

Figure 5 – Comparison of the coprecipitation and the thermal decomposition methods, according to shape and size distribution.

In principle, thermal decomposition strategies can be subdivided into hot-injection approaches, where the precursors are injected into a hot reaction mixture, and conventional reaction strategies where a reaction mixture is prepared at room temperature and then heated in a closed or open reaction vessel. Thermal decomposition methods yield highly crystalline magnetic iron oxide nanoparticles with a narrow size distribution, through the complete separation of the nucleation and

growth steps [47]. Iron precursors, such as Fe(acac) (III) or Fe(oleate)$_3$, have been constantly used to produce monodisperse iron oxide nanoparticles through thermal decomposition methods [14]. These iron oxide nanoparticles have been reported by several researchers as potential nanomaterials for biomedical applications [3, 16, 17].

Synthesis of Fe_3O_4 nanoparticles

This synthesis was adapted from a previously reported one by Guardia et al [3]. In a round bottom flask, 0.7190 g of Fe(acac) (III) and 2.332 g of Decanoic Acid were mixed in 50 mL of Dibenzyl Ether. The mixture was purged in vacuum during 1 hour at 20 °C, and then placed under a Nitrogen atmosphere. The mixture was then heated until 200 °C during 2 hours, with an heating rate of 6 °C/minute. The temperature was later increased until reflux was observed (around 275 °C) during 1 hour, and then cooled until room temperature. The nanoparticles were collected through centrifugation and washed with a mixture of ethanol/hexane (2:1). The nanoparticles were later dried and collected for storage.

X-Ray Diffraction

X-ray diffraction (XRD) is an analytical technique based on the coherent constructive interference of X-rays and is used for the study of numerous materials, which allows the identification of the crystalline phases present on the material, as well as the existence of amorphous material. In the case of crystalline phases, this technique can give information about the dimensions of the unit cell, the existence of nanocrystalline material, the existence of deformations within the lattice, and so on [61].

The Rietveld refinement method was developed for curve fitting of the entire powder diffraction profile and to allow the extraction of the maximum possible information. This technique has had a significant impact on various materials sciences. Specifically on nanomaterials, Rietveld allows, for example, the refinement of lattice parameters, the detection of distortions, the presence of tensions and the finite size effect. Figure 6 shows an X-ray Diffractogram of a Fe_3O_4 sample, its Rietveld Refinement and the corresponding unit cell drawing. Rietveld Refinement was performed using the Software FullProf Suite© which also gave the necessary information to draw the unit cell on Software VESTA©[1]. The X-ray diffractogram presents a typical diffraction pattern of Fe_3O_4 nanoparticles showing the fingerprint peaks of Fe_3O_4. Some small differences between the experimental and the refined data can be noticed. These may appear due

[1]FullProf Suite© official website: www.ill.eu/sites/fullprof/
VESTA© official website: jp-minerals.org/vesta/en/

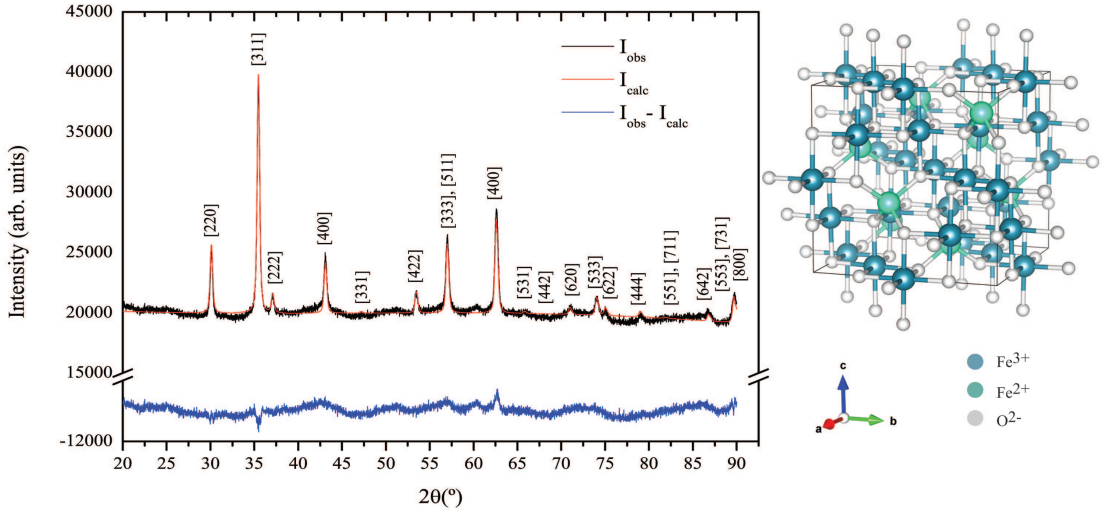

Figure 6 – X-Ray Diffractogram of Fe_3O_4 nanoparticles and proposed unit cell. The black line corresponds to the experimental data collected, the red line represents the obtained Rietveld refinement and the blue line shows the mathematical difference between the other two.

Table 2 – Dimensions of the Fe_3O_4 cubic unit cell.

	Bulk [62]	Refined
a, b, c	8.3916(2) Å	8.3915(2) Å

to small initial reagents or residues that could not be separated during the washing process of the nanoparticles.

Using the Rietveld Refinement it was possible to refine lattice parameters, which are presented in Table 2. The average apparent size on the Fe_3O_4 sample obtained was 24 nm. The size effects were treated with the integral breadth method using the Voigt model for both the instrumental and intrinsic diffraction peak shape considering a Thompson-Cox-Hastings pseudo-Voigt convoluted with Axial divergence asymmetry function to describe the peak shape. The contribution of the instrument to the peaks broadening was determined by the refinement of the XRD pattern of a LaB6 standard sample (NIST ref. 660a).

Infrared Spectroscopy

Infrared Spectroscopy is a commonly used technique to detect the vibration frequencies of several types of bonds [63]. Fe_3O_4 nanoparticles were analysed through Infrared Spectroscopy between 4000 and 350 cm^{-1} and the resulting spectra is presented in Figure 7. The observed peaks at 650 cm^{-1} and 560 cm^{-1} were assigned to the stretching vibration (ν) between the atoms of Fe and O in the crystalline lattice of Fe_3O_4.

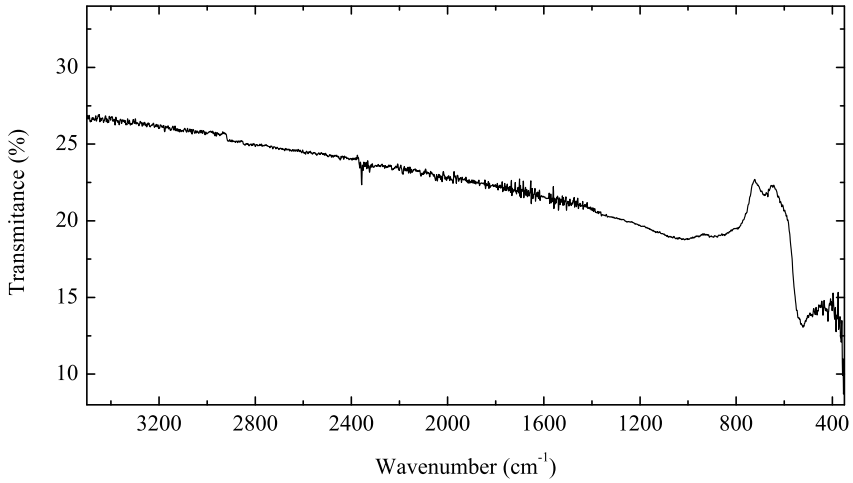

Figure 7 – Infrared Spectra of Fe_3O_4 nanoparticles using the Attenuated Total Reflectance mode.

Transmission Electron Microscopy

In order to observe the morphology of the nanoparticles, Transmission Electron Microscopy (TEM) was used and the size of the nanoparticles was later determined using the ImageJ© software. TEM images of the Fe_3O_4 nanoparticles are shown in Figure 8. From the TEM images, it can be concluded that the nanoparticles have a narrowed size distribution centred around 17 nm, and a great control over shape. This value is close to the average apparent size obtained from the Rietveld Refinement, 24 nm, and this difference can be due to the fact that the XRD analysed Fe_3O_4 nanoparticles were not from the same batch as the TEM analysed Fe_3O_4 nanoparticles.

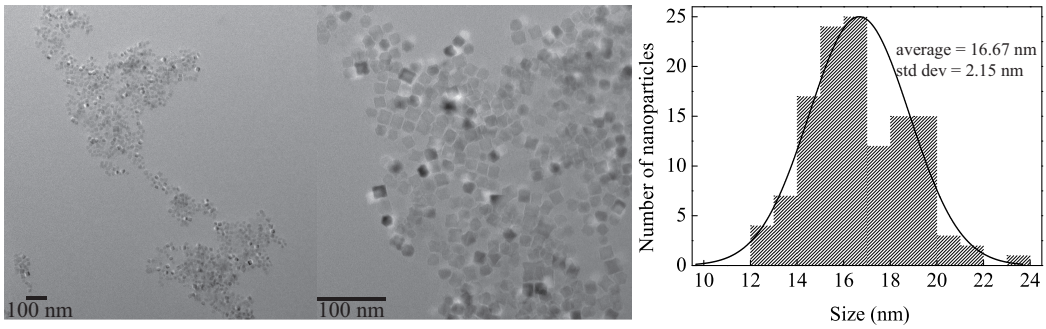

Figure 8 – Transmission Electron Microscopy images of Fe_3O_4 nanoparticles.

2.2 Fe_3Se_4 nanoparticles

Iron selenides are a family of compounds with a wide range of magnetic properties and compositions, including the diamagnetic $FeSe_2$, the ferrimagnetic Fe_3Se_4 and Fe_7Se_8, and the antiferromagnetic (and superconductor) FeSe [64]. This rich phase diagram results in the first hurdle to be overcome while designing of a successful chemical route for the synthesis of iron selenide nanocrystals: phase purity. The iron/selenium phase diagram shows that the most Se-rich phase, $FeSe_2$, and mixtures of $FeSe_2$ and Fe_3Se_4 are the most stable at lower temperatures, while the less Se-rich phases are stable at higher temperatures, and Fe_3Se_4 forms at intermediate ones [65]. This means that, if while aiming to design a route where reactants are mixed at ambient temperature, the system would cross thermodynamic conditions that favour the formation of $FeSe_2$ before reaching the conditions for the formation of Fe_3Se_4 [64]. The use of a hot-injection route where Fe and Se precursors are mixed above the typical nucleation temperature $FeSe_2$ would avoid this problem [65]. However, a "ramped" route where all reactants are mixed at room temperature is preferably to a hot-injection route, due to to being a safer and more reproducible method.

When performing a thermal decomposition method to synthesize Fe_3Se_4 nanoparticles, it is necessary to choose an iron and a selenium precursor. A Selenium-Octadecene (Se-ODC) metal-organic complex was selected due to its reactivity and stability [66]. Several reactional times and different proportions were evaluated, and it was noticed that the reaction time of synthesis of this precursor affected the phase purity of Fe_3Se_4 nanoparticles. Metal-organic iron complexes are included in the most used iron precursors for nanoparticle synthesis [14]. Among these, Fe(acac) (III) and $Fe(oleate)_3$ were considered good candidates for this synthesis. Unfortunately, $Fe(oleate)_3$ is a multi-step synthesis precursor, i.e., starting with $FeCl_3$ and reacting with sodium oleate, this precursor is synthesized and then submitted to a drying process that cannot be easily repeated. The final synthesis step of this precursor yields a caramel-like compound, which is difficult to weight and manage. This leads to a huge amount of human error, and reproducibility is compromised. Thus, it was decided to move forward and explore Fe(acac) (III) as an iron precursor, due to its proven advantages: it is a commercial powder precursor, it is easy to manipulate, and the results are reproducible.

In the scope of this thesis, synthetic conditions, for iron selenide nanoparticles (Fe_3Se_4), were optimized based on Fe(acac) (III). In fact, the optimization process included about

80 synthesis of these nanoparticles. Below are described the selected synthesis of the Selenium precursor (Se-ODC) and the Fe_3Se_4 nanoparticles.

Synthesis of Se-ODC

This synthesis was adapted from a previously reported one by Bullen et al [66]. In a round bottom flask, 283 mg of Selenium Powder were dissolved in 154 g of Octadecene. The mixture was purged under vacuum at 120 °C. After 1 hour, the mixture was then placed under a Nitrogen Atmosphere and the temperature was increased to 215 °C. After 10 minutes the reaction was cooled to room temperature and reserved in a flask for further usage.

Synthesis of Fe_3Se_4 nanoparticles

In a round bottom flask, 58.5 mg of Fe(acac) (III), 10.2809 g of Se-ODC, 15.3 mg of 1-Dodecanethiol (DDT) and 23.7 mg of Tetradecylphosphonic acid (TDPA) were mixed and purged in vacuum at 70 °C. After 1 hour, the mixture was placed under a Nitrogen atmosphere and heated up to 250 °C during 30 minutes with an heating rate of 5 °C/minute. The reaction was then cooled until room temperature and the nanoparticles were washed with hexane, collect through centrifugation and dried for storage.

X-Ray Diffraction

Similarly to the characterization of Fe_3O_4, the X-ray Diffraction technique was used in order to determine the present phase on the Fe_3Se_4 sample. Rietveld Refinement was performed using the Software FullProf Suite© which also gave the necessary information to draw the unit cell on Software VESTA©. The X-ray diffractogram shows a typical diffraction pattern of Fe_3Se_4. The Rietveld Refinement allows the possibility of refining important values such as lattice parameters, which are compared to bulk values in Table 3. After the refinement, the average apparent size obtained for the Fe_3Se_4 sample was 56.1 nm. In this case, the apparent sized cannot be considered the nanoparticle size due to the fact that these nanoparticles come in the form of multidomain. These results show that the nanoparticle unit cell does not suffer from distortion as much as the bulk unit cell.

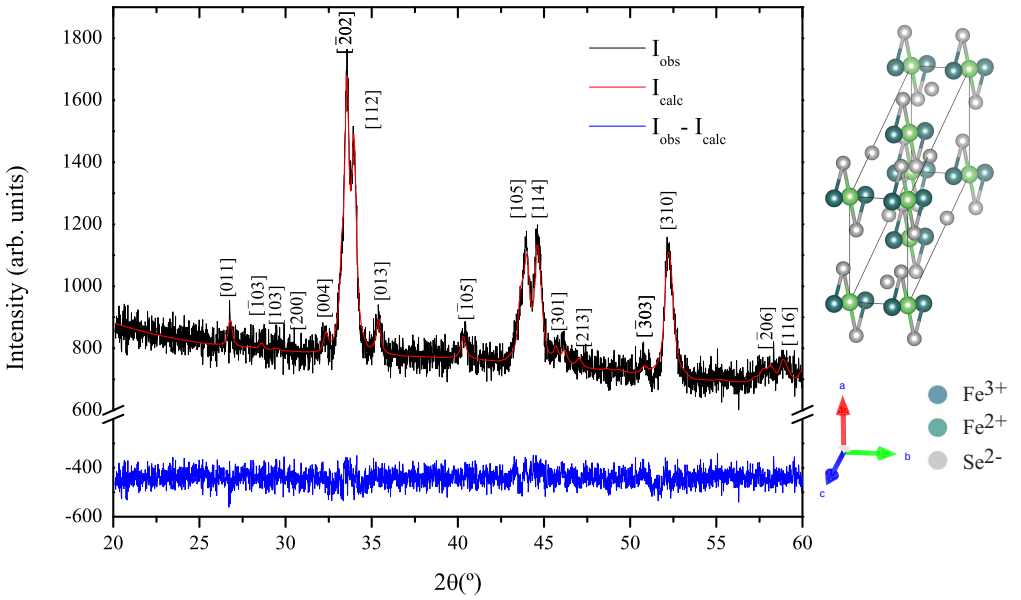

Figure 9 – X-Ray Diffractogram of Fe_3Se_4 nanoparticles and proposed unit cell.

Table 3 – Dimensions of the Fe_3Se_4 monoclinic unit cell.

	Bulk [67]	Refined
a	6.208(2) Å	6.160(3)Å
b	3.541(1) Å	3.532(2)Å
c	11.281(3) Å	11.205(8)Å
α	90.00°	90.00°
β	91.80°	91.50°
γ	90.00°	90.00°

Infrared Spectroscopy

The Infrared spectrum of Fe_3Se_4 nanoparticles is presented in Figure 10, between 3500 cm^{-1} and 450 cm^{-1}. The observed peaks at 2921 cm^{-1} and 2849 cm^{-1} were assigned to the stretching vibration (ν) of the O-H link typically present in carboxylic acids. At 1710 cm^{-1} it was detected the presence of a small stretching vibration (ν) of the C=O link, commonly observed on carboxylic acids. At 980 cm^{-1} a C-O stretching vibration appeared, which was also another signal of the presence of the carboxylic group. Although this seems odd, the presence of the carboxylic group can derive from a surface stabilizer that forms during the synthesis.

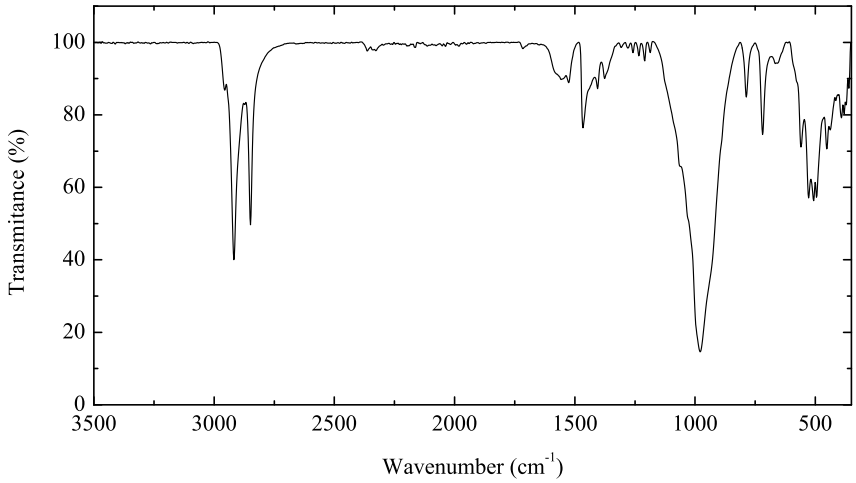

Figure 10 – Infrared Spectra of Fe_3Se_4 nanoparticles using the Attenuated Total Reflectance mode.

Transmission Electron Microscopy

In order to observe the nanoparticles, Transmission Electron Microscopy (TEM) was used and the size of the nanoparticles was later determined using the ImageJ© software. TEM images of the Fe_3Se_4 sample are shown Figure 11. From the TEM images, it can be concluded that the nanoparticles have a larger size distribution than that observed in Fe_3O_4 nanoparticles, centred around 350 nm, and a great control over shape.

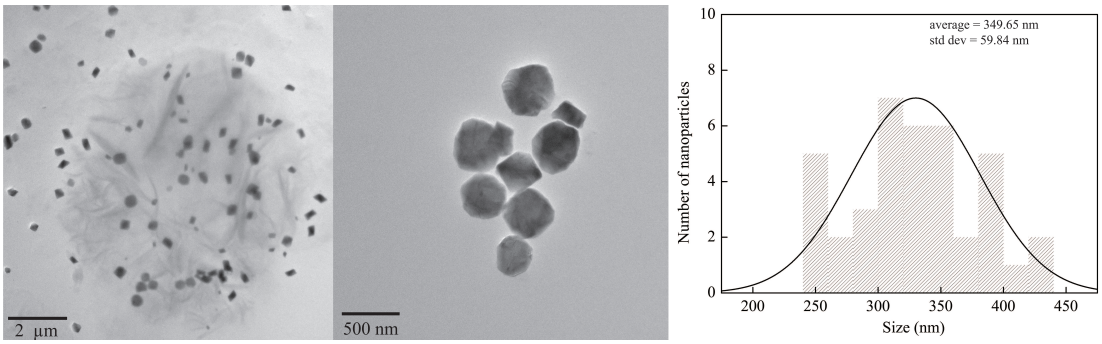

Figure 11 – Transmission Electron Microscopy images of Fe_3Se_4 nanoparticles.

2.3 Surface functionalization of magnetic nanoparticles

As mentioned before, thermal decomposition methods imply the synthesis of hydrophobic nanoparticles, which can be considered a disadvantage for biomedical applications [56]. Hence, it is necessary to perform a hydrophobic-hydrophilic phase exchange or some sort

of surface coating. Often, surface coatings are used to achieve a specific functionalization [68].

Functionalization strategies usually consist on a first step which aims at covering the surface with reactive groups (amino, carboxylates, thiols, aldehydes) so as to ensure, at the second step, the further coupling of biomolecules of interest such as streptavidin or antibodies. Some strategies include polymers, proteins, protein-resistant MR probes and hyaluronic acid layers [69]. Although, these surface coatings are usually thick, which increases the total radius of the nanoparticles. Specially in biomedicine, the size of nanoparticles can affect the success of its application. Thus, it is common to look for alternatives that allow: (1) a simple functionalization method and (2) a coating that does not add much size to the nanoparticles [70]. With that in mind, scientists have previously developed catechol-based biomolecules to anchor onto the surface of nanoparticles [71, 72]. This strategy relies on the chemical anchoring of hydroxyl groups (-OH) onto the surface of Fe_3O_4 nanoparticles, leaving different organic groups at the surface available for further linkages. For example, in the case of caffeic acid, the nanoparticles would be functionalized with carboxylic groups (-COOH), whilst in dopamine would be functionalized with amines ($-NH_2$). This allows the possibility of a one-step phase exchange and functionalization with small biomolecules, decreasing the time and resources used in these processes when compared with the typical two-step method. Although, these methods tend to use organic solvents (tetrahydrofuran), which should be avoided as possible, following the Green Chemistry principles, as a way to reduce toxicity of the final product and the obtained waste [73]. These methods have been adapted in terms of proportions and the choice of solvent (ethanol) in the scope of this thesis that led to de development of several different functionalizations as shown in Figure 12.

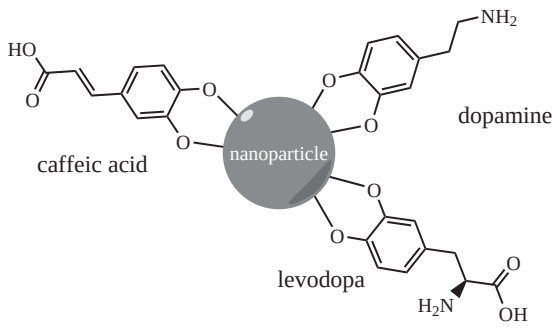

Figure 12 – Possible alternative surface functionalizations of nanoparticles with small biomolecules with catechol groups: caffeic acid, dopamine and levodopa.

As will be explored in Chapter 3: Applications, iron oxide nanoparticles can be used as T_2 contrast agents for MRI. Since amines can bind to known T_1 contrast agents such as Gd-DTPA, the idea of combining dopamine and levodopa with such agents could lead to a functionalized surface in only one step and the development of a T_1/T_2 contrast agent.

One-step Phase Exchange and Functionalization

Synthesis

Nanoparticles were dispersed in ethanol with the help of an ultrasonic bath. Then, the surface agent was added, and the mixture was left stirring under Nitrogen at 50 °C for 3 hours. The resulted mixture was then cooled and collected. The functionalized nanoparticles were collected, washed 2 times with ethanol, and then dried in a fume hood. After adding 2 mL of water and leaving a few minutes dispersing inside an ultrasonic bath, the particles appeared to be stable in water. Of course, as in any experimental method, this was not verified 100 % of the time. It was noticed that the stabilization in water after the procedure often depends on the initial state of the nanoparticles, i.e., the longer the nanoparticles were storaged, the more difficult would be to succeed in this methodology.

The quantities of nanoparticles, surface agent and ethanol varied according to the case:

- A dopamine functionalization was achieved mixing 10 mg of nanoparticles, 50 mg of dopamine hydrochloride and 10 mL of ethanol.
- A levodopa functionalization included 10 mg of nanoparticles, 60 mg of levodopa and 10 mL of ethanol.

Zeta Potential

Zeta Potential was performed at a neutral pH in order to determine the surface charge of the nanoparticles. Table 4 shows the results of the two types of nanoparticles with the different functionalizations. These results show that nanoparticles coated with dopamine present a positive (+) charge, which is consistent with the premise that, in this case, amine groups are left available at the surface of the nanoparticles. The amine group ($-NH_2$) can be easily protonated ($-NH_3^+$), when in an aqueous solution, thus conferring a positive charge to the prepared nanoparticles. The nanoparticles coated with levodopa present a negative (-) charge, which supports the premise that carboxylic groups (-COOH) are available at the surface of the nanoparticles. The carboxylic group (-COOH)

can be easily deprotonated (-COO^-), when in an aqueous solution, thus conferring a negative charge to the prepared nanoparticles.

Table 4 – Zeta Potential values for nanoparticles with different coatings.

Sample	Zeta Potential (mV)
Fe_3Se_4@Dopamine	+3
Fe_3Se_4@Levodopa	-20
Fe_3O_4@Dopamine	+32
Fe_3O_4@Levodopa	-18

3. Applications

This Chapter describes the two applications explored in the scope of this thesis: (1) Logic Gates for a threshold temperature control and (2) contrast agents for Magnetic Resonance Imaging. First, a state of the art is presented, then the experimental part is described and the results are discussed. The first application was developed in collaboration with Dr. Vítor Gaspar and Professor João Mano.

3.1 Temperature threshold in hyperthermia

Temperature is one of the most important parameters in our daily life. For instance, when transporting food, there are certain temperature limits that should not be crossed [74, 75]. Also in medicine, hyperthermia treatments require temperature ranges that cannot easily be detected *in situ*. It is, then, critical to know at what dose does the temperature increase locally, above a given threshold [76].

Hyperthermia treatments increase the local temperature of the tumour region to about 42-46 °C, in which cancer cells can be selectively damaged without much harm to the healthy surrounding tissue. If the temperature goes up above 46 °C, which is known as thermal ablation, this may result directly in complete necrosis of the cells [10]. Therefore, the development of temperature monitoring systems that are able to give information about exceeding these defined thresholds is a significant part of research. Regarding this, thermoresponsive nanothermometers have been developed to measure, for example, temperature variations inside living cells [77]. However, many drawbacks still limit the practicability and thus the usefulness of these approaches. These limitations include poor biocompatibility, low-temperature resolution, slow response time, complex synthesis, expensive instrumentation and complex nonlinear responses [78].

Furthermore, temperature monitoring systems can also be based on a set/reset flip-flop logic gate (SR-latch) that responds to temperature as one of the inputs. This gate changes state as soon as the temperature increases above a defined threshold and

keeps memory of that event, even after the temperature drops. The gate remains in this state until a second kind of input resets it back to the original state. One of the advantages of devices based on this gate is having a short response time, however they can only determine if the temperature exceeds a defined threshold, not the exact value of temperature. Magnetic materials can act as SR-latches due to their natural display of bisatble responses. Useful materials in this context have a net magnetic moment whose direction is difficult to change with an external field. Such materials are generally termed "hard magnets", in opposition to "soft magnets", where the net magnetic moment can easily follow the external field [79].

3.1.1 Fe_3Se_4 nanoparticles as logic gates

Fe_3Se_4 nanoparticles are considered hard magnets and have a magnetic phase transition slightly above room temperature, which causes the particle to lose its ferrimagnetic arrangement. The temperature at which this phase transition occurs is called Curie temperature (T_C), and can vary according to several parameters, for example, the size and crystallinity of the nanoparticle. As observed in Figures 13 (a) and (b), T_C tends to increase according to the crystallite size determined by XRD, as usually found in finite-size systems.

Below T_C the nanoparticles present an hysteretic behaviour, allowing the magnetization to assume several different values according to the temperature and magnetic field history of the material. Figure 13 (c) shows the magnetization recorded as a function of temperature after cooling above T_C (60 °C) with (FC) or without (ZFC) an applied magnetic field. Below 35 °C the curves diverge, and the system is in a high or a low state, respectively. Above 35 °C the system loses its ferrimagnetic arrangement and remanent magnetization. Thus, below T_C the system can be in, at least, two different states, which depend on the history of the applied magnetic field and temperature. Above T_C only one state is possible. This fact allows the design of a logic gate that: (1) if cooled without an applied field is set to a low state; (2) if cooled with an applied magnetic field is set to a high state. The input "magnetic field" will take this system from a low to a high state, and the input "temperature" will always lead the system to a low state. This magnetic behaviour allows Fe_3Se_4 nanoparticles to act as a bi-stable gate, according to the latest applied stimuli: magnetic field or temperature. The gate can be represented by two NOR elements in feedback, with two possible inputs, a set (S) and a reset (R), and one output (Q or $\bar{Q}$) (Figure 2).

Figure 14 shows the time diagram of the proposed logic gate. Initially, the system was

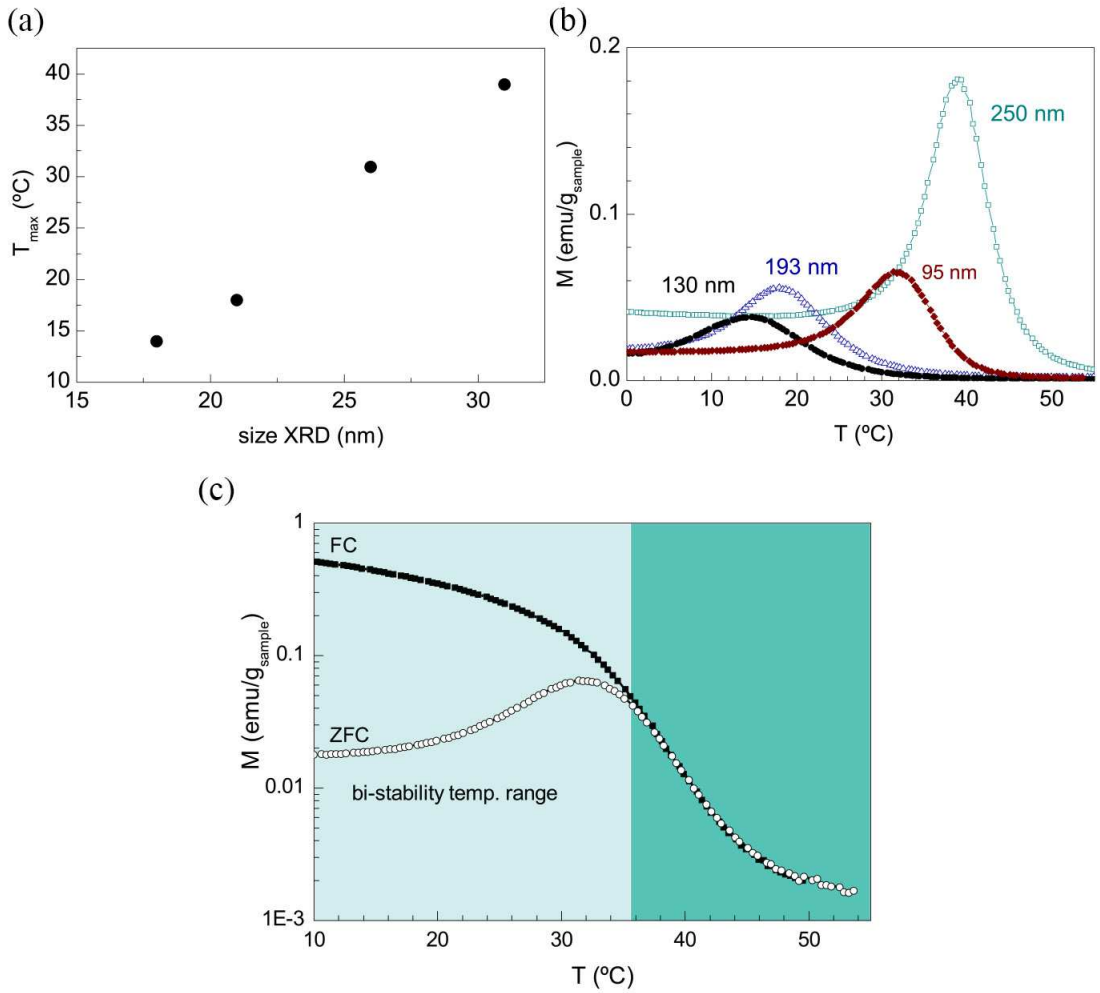

Figure 13 – **(a)** Average apparent sizes obtained from Rietveld refinement as a function of T_C; **(b)** ZFC Magnetization of Fe_3Se_4 nanoparticles with different average diameter as a function of T_C; **(c)** Standard zero-field cooling (ZFC) and field cooling curves (FC) of Fe_3Se_4 nanoparticles.

in a low state, which was followed by the application of a magnetic field. This field led the system into a high state. When the field is removed, the system remains in a high state due to its hard magnetism, leaving a remanent magnetization. Afterwards, temperature was raised, which caused the magnetization to drop until a low state was achieved. When temperature dropped, the system remained in a low state. After this first sequence, the time diagram shows several other sequences which show that a smaller variation of temperature achieves the same result. This behaviour mimics one of a SR-latch, using the magnetic field to set the system into high state and temperature to set the system into a low state. A true table of the proposed SR-latch is presented on Table 1.

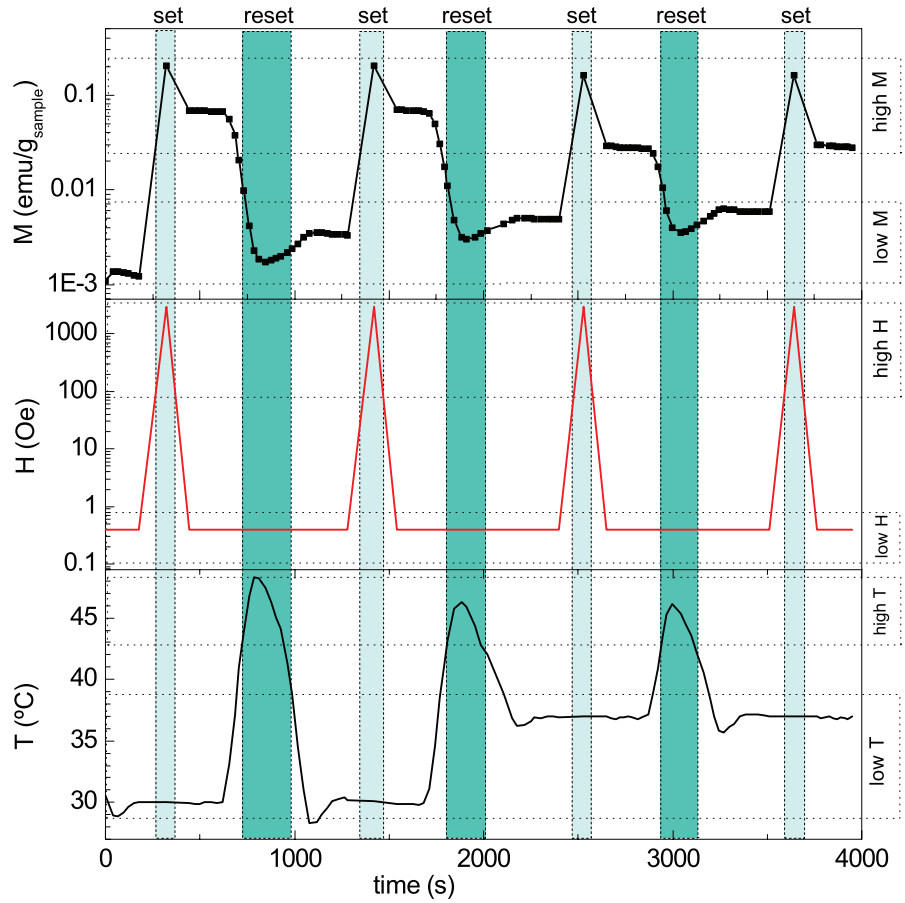

Figure 14 – Set and reset sequences of Fe_3Se_4 nanoparticles

3.1.2 Logic gates in cell cultures

Hard magnetic nanocrystals with T_C close to room temperature, such as the Fe_3Se_4 nanoparticles here presented, can give valuable insight into materials and systems which are sensitive in the same temperature range, such as tissues, cells, biomolecules and soft materials in general. For instance, Fe_3Se_4 nanoparticles with a T_C close to 40 °C can record information of an event of temperature increase above the normal cell temperature. Below T_C, i.e., in the normal temperature range, the nanoparticles may have a stable high or a stable low value of the remanent magnetization, M_r, (being the difference between both at least an order of magnitude), depending on which stimuli was applied last: a magnetic field or a temperature above T_C, respectively.

After setting the Fe_3Se_4 nanoparticles into a high state by the application of a magnetic field, a temperature increase above the threshold defined by T_C will reset M_r into a low state, thus recording information about that increase. After reading this information,

the nanoparticles can be set again in a high state, which can be easily performed with an external magnetic field. This corresponds to a logic gate where temperature and field are the input stimuli and remanent magnetization is the output, being this gate able to answer the question "did the temperature went above the threshold defined by T_C since the last time we applied an external field?". In the context of cells, this question arises, for instance, after the application of targeted hyperthermia, where heat sources placed close to or inside cells are triggered at distance.

In order to evaluate the behaviour of these nanoparticles as SR-latches in living cells, an experimental procedure was carried out. Prostate cancer cells (PC-3) were routinely cultured and grown in cell culture in a temperature-controlled incubator at 37 °C, 5 % CO_2 and in a humidified atmosphere, by Dr. Vítor Gaspar. μ-slide angiogenesis Ibidi imaging chambers were coated with a nanoparticle suspension until a uniform layer was formed. Subsequently, Matrigel^{TM} was deposited on top of the nanoparticle layer and allowed to crosslink at 37 °C for 2 hours. This dual deposition strategy allowed for the formation of a cell adhesive substrate for PC-3 cells proliferation. Prostate cancer cells were then seeded and allowed to proliferate during 24 hours. Irradiation was performed using a 850 nm Near Infrared LED with a power density between 228 and 570 mW/cm^2 during 5 minutes. The Fe_3Se_4 nanoparticles on the wells were magnetized (set in the high state) using a typical neodymium-iron-boron magnet. The states before and after the irradiation procedures were measured using a fluxgate magnetometer embedded in a permalloy foil to decrease the ambient magnetic field and noise at the fluxgate. After irradiation, cells were incubated for 24 hours at 37 °C. The cells were then washed and imaged. The graphical explanation of this methodology as well as the resulting fluorescence microscopy images are presented in Figure 15.

It was observed that for a total irradiation time of 5 minutes, the logic gates indicated that the temperature threshold of 42 °C was crossed for power densities between the 456 and 570 mW/cm^2 range (Figure 16). As observed in Figure 15, the majority of cells subjected to a temperature below the threshold of the nanoparticles (<42 °C) were viable. When cells were subjected to a temperature above the threshold of the nanoparticles (>42 °C), the results show the opposite. These results highlight the use of the Fe_3Se_4 nanoparticles to simultaneously gain insight as a quality control technology for temperature thresholds during treatments, while acting as NIR light absorbers in anti-cancer hyperthermia. This insight can be explored in temperature control devices for hyperthermia cellular assays in cell plates, or, if further studied, in nanothermometers. In an ideal method, the nanoparticles would have been placed near

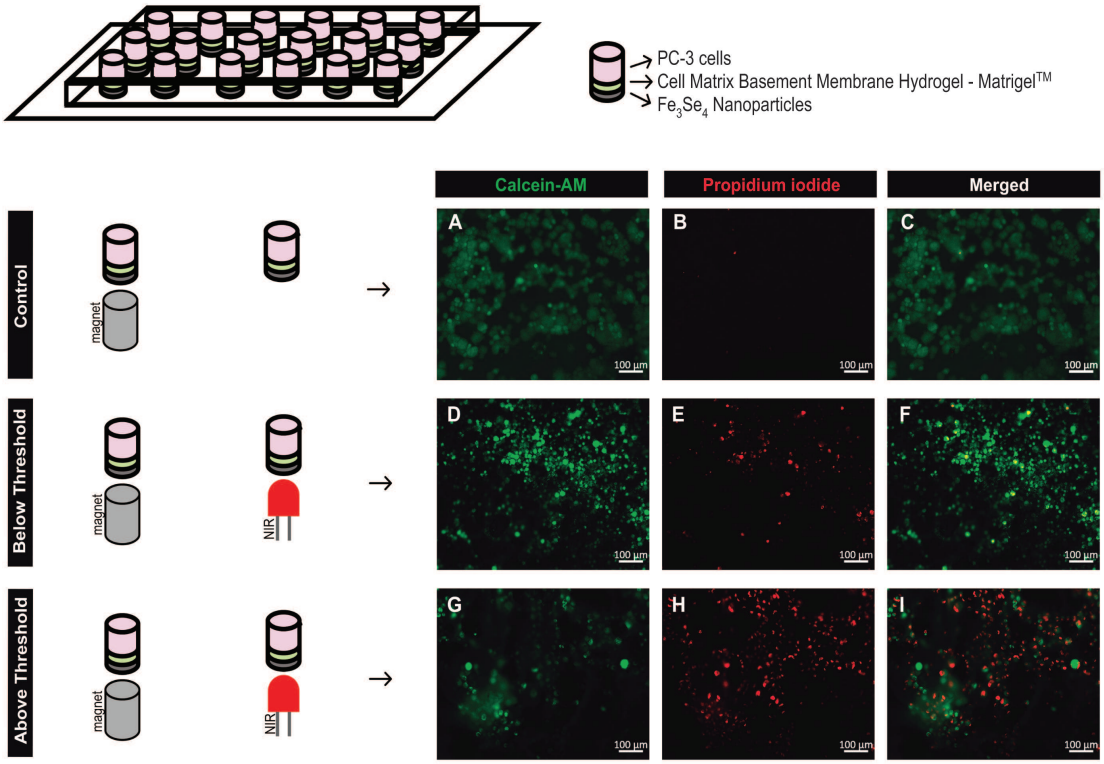

Figure 15 – Scheme of the use of the logic gates to record a possible overcome of the 42 °C threshold temperature during irradiation and fluorescence microscopy micrographs of irradiated PC-3 cells.

the targeted tumour or tissue, and the magnetic signal would have been detected during the heating process. When M_r would have reach its typical minimum value for Fe_3Se_4 nanoparticles (determined before the beginning of the treatment), the heating would have stopped, and the treatment would have been specific to unhealthy tissues or cells, and would have not affected healthy ones.

Several other methods are left to explore, such as the combination of Fe_3Se_4 nanoparticles with Fe_3O_4 nanoparticles, where the first ones would act as nanothermometers, whilst the last ones would act as the heating source through magnetic hyperthermia. It is thought that Fe_3O_4 nanoparticles tend to heat more than Fe_3Se_4 nanoparticles, and so, with a small amount of Fe_3O_4 nanoparticles, the heating could be more effective and the nanoparticle dose could be smaller. One of the advantages of this combination is that the Fe_3O_4 nanoparticles are less dangerous to the environment than Fe_3Se_4, as will be discussed in Chapter 4: Biological Evaluation, which means that this combination, where Fe_3Se_4 nanoparticles are used as a sensor and not as an heating source, could be safer for the environment and the patient.

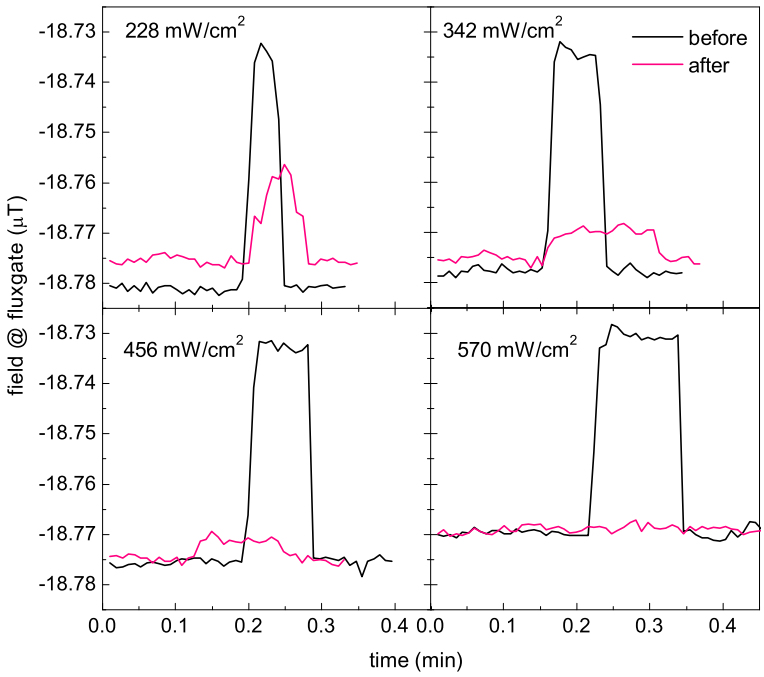

Figure 16 – Remanent magnetization M_r measured by the fluxgate magnetometer on the cell wells before and after irradiation with a given power during 5 minutes.

3.2 Contrast agents for MRI

As mentioned before, the process of relaxation is a function of the water proton environment and varies according to the tissues. The signal depends on the concentration of protons and on nuclear relaxation times, T_1 and T_2. The last can be affected by contrast agents, depending on its intrinsic magnetic properties [48].

Contrast agents decrease the proton relaxation time thus reducing the acquisition time of the image. Contrast agents can be made of paramagnetic or superparamagnetic materials. Paramagnetic contrast agents usually shorten T_1 and superparamagnetic contrast agents affect mainly T_2. Typically, T_1 contrast agents, available in the market, contain Gd^{3+} complexes, such as Gd-DTPA, and T_2 contrast agents are made of iron oxide nanoparticles coated with Dextran [47, 49].

As mentioned before, a new generation of contrast agents comprises the combination of paramagnetic and superparamagnetic centres, to achieve a situation where both T_1 and T_2 can be actuated. Some materials have been developed for this purpose, yet, the combinations of the two magnetic centres tend to be performed in several steps, which implies more reactions, resources, and time.

In the scope of this thesis different types of Gd^{3+} functionalized Fe_3O_4 nanoparticles were developed to act as a dual-mode contrast agents for MRI. This was achieved through the surface functionalization of these nanoparticles with new organic Gd^{3+} complexes that result from a modification of the know Gd-DTPA complex: the carboxylic groups of DTPA reacted with levodopa and dopamine, two known amines. The advantage of using dopamine and levodopa as substitutes for the carboxylic groups relies on the fact that these two biomolecules are part of the catechol family, which, as explained before promotes the linkage onto the surface of iron oxide nanoparticles, through the hydroxyl groups (-OH).

In addition to the dual-mode contrast agents, iron selenide nanoparticles were also evaluated as T_2 contrast agents due to magnetic phase transition near room temperature.

In the frame of this application several tasks were performed, namely the nanoparticle synthesis in organic medium - which was described in the Chapter 2: Synthesis and Characterization -, to guarantee a controlled shape and size distribution; and organic-aqueous phase transfer and functionalization with Gd^{3+} complexes, achieved by the linkage of small catechol based molecules onto the surface of the nanoparticles, in an one step methodology.

The graphical abstract of the proposed synthesis for dual-mode contrast agents is presented in Figure 17.

3.2.1 T_1 contrast agents

Gd^{3+} based contrast agents

Gadolinium is very toxic in its hydrated form $[Gd(H_2O)_8]^{3+}$. The leaking risk and toxic of Gd^{3+} ions, the low relaxivity and the short half-lives of the compounds limit the application of Gd^{3+}-based agents. To avoid toxicity while maintaining the magnetic and electronic properties of this ion, paramagnetic Gadolinium complexes have been used. Further, the ligand complexation to the metal has to leave free coordination sites so that one or several molecules of water can link to the metal, thus increasing the relaxivity. The first Gadolinium complexes commercially available were Magnevist® (Gd-DTPA) and Dotarem® (Gd-DOTA). There are other DTPA derivatives currently being developed, which can soon turn into new contrast agents when complexed with Gd. Mainly, these derivatives are synthesized through a general reaction between DTPA and an amine, as shown in Figure 18 [80]. From this typical DTPA-bisamine synthesis,

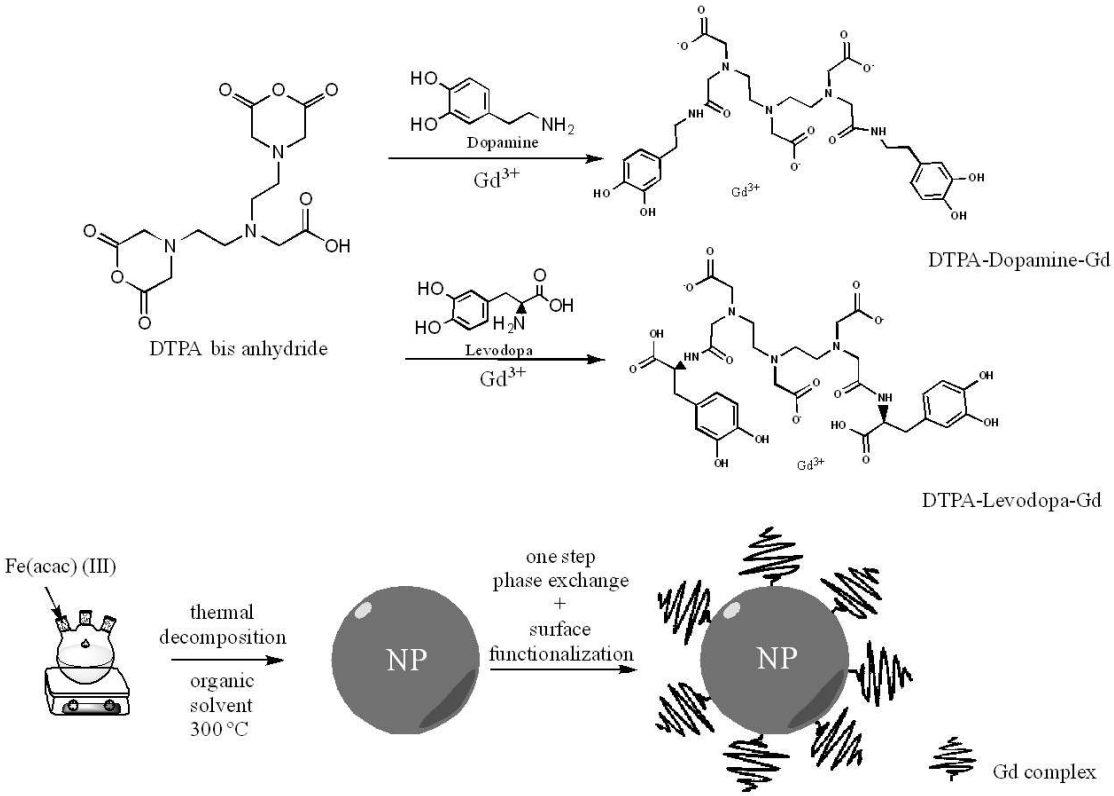

Figure 17 – Organic synthesis of Gd^{3+} complexes and surface functionalization of nanoparticles.

the idea of combining a molecule with amines and catechol groups appeared in order to link Gd-DTPA derivatives onto the surface of Fe_3O_4 nanoparticles through the hydroxyl groups (-OH) [81]. Two catecholamines were selected for this purpose: dopamine and levodopa. Below the synthesis for the preparation of the Gadolinium complexes are described, as well as the used characterization techniques.

Synthesis of DTPA-bisanhydride

In a flask, 15.734 g of DTPA, 16.4788 g of acetic anhydride and 20 mL of pyridine were added. The mixture was then heated up to 65 °C during 24 hours in an open atmosphere. After the reaction, the product was filtered under vacuum and washed twice with the following procedure: 3×40 mL of acetic anhydride and 60 mL of acetonitrile. The obtained solid was then dried overnight in an oven set at 60 °C, yielding a white solid.

Elemental Analysis: 45.14 % Carbon, 5.12 % Hydrogen, 11.33 % Nitrogen.

^{13}C NMR (Solid State, 400, 12 kHz): δ 44 (c), δ 52 (d), δ 53 - δ 54 (e), δ 57 (b), δ 168.5 (a), δ 171.1 - δ 175 (f). This represents a tentative to propose the peak assignments. The spectra and structure of this compound is shown in Figure A1.

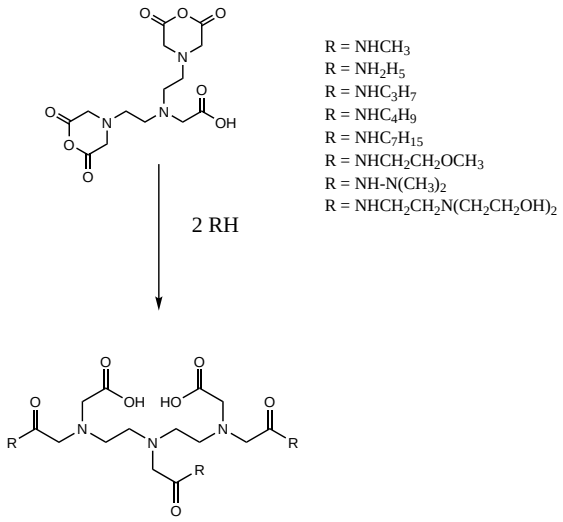

Figure 18 – Synthesis of DTPA-bisamine derivatives.

Synthesis of DTPA-bisdopamine

In a flask, 2.5624 g of dopamine • HCl and 2.8336 g of the DTPA-bisanhydride previously prepared were dissolved in 200 mL of distilled water and heated up to 50 °C during 5 hours at an open atmosphere. After the reaction, the mixture was left in a glass until precipitation was observed (3-5 days). The precipitated was then centrifuged and dry in an oven set between 40 and 60 °C and later collected to storage.

Elemental Analysis: 42.70 % Carbon, 5.65 % Hydrogen, 10.34 % Nitrogen.

^{13}**C NMR** (Solid State, 400, 12 kHz): δ 44 (*j*), δ 52.5 - δ 61 (*b*, *c*, *d*, *e*, *g*, *i*), δ 116 - δ 122.5 (*k*, *l*, *o*, *p*, *q*), δ 142 - δ 145 (*m*, *n*), δ 168.5 - δ 175.5 (*a*, *f*, *h*). This represents a tentative to propose the peak assignments. The spectra and structure of this compound is shown in Figure A2.

Synthesis of DTPA-bislevodopa

In a flask, 2.5624 g of levodopa and 2.8336 g of the DTPA-bisanhydride previously prepared were dissolved in 200 mL of distilled water and heated up to 50 °C during 5 hours at an open atmosphere. After the reaction, the mixture was left in a glass until precipitation was observed (3-5 days). The precipitated was then centrifuged and dry in an oven set between 40 and 60 °C and later collected to storage.

Elemental Analysis: 48.65 % C, 5.46 % H, 9.01 % N.

^{13}**C NMR** (Solid State, 400, 12 kHz): δ 37 - δ 53 (*b*, *c*, *d*, *k*), δ 54 - δ 61 (*e*, *g*, *j*), δ 115.5 - δ 127 (*l*, *m*, *n*, *p*, *q*), δ 143 - δ 144 (*o*, *n*), δ 168.5 - δ 177 (*a*, *f*, *h*, *i*). This represents a

tentative to propose the peak assignments. The spectra and structure of this compound is shown in Figure A3.

Gadolinium Complexation

1.5 g of $GdCl_3 \bullet 6\ H_2O$ and 3 g of the previously prepared DTPA bis amine were dissolved in 90 mL of distilled water. The pH was adjusted to 5.8 and the reaction was carried out at 70 °C during 3 hours. After the reaction, the mixture was left in a glass until precipitation was observed (3-5 days). The precipitated was then centrifuged and dry in an oven set between 40 and 60 °C (during 1 week) and later collected to storage.

Infrared Spectroscopy

Infrared Spectroscopy was performed as a complementary characterization technique in order to identify organic groups and also to be able to detect differences between vibrational modes on different compounds.

Figure 19 shows two groups of Infrared spectra. On the left, Dopamine derivatives of DTPA and the corresponding Gadolinium complex. The main bands that stand out

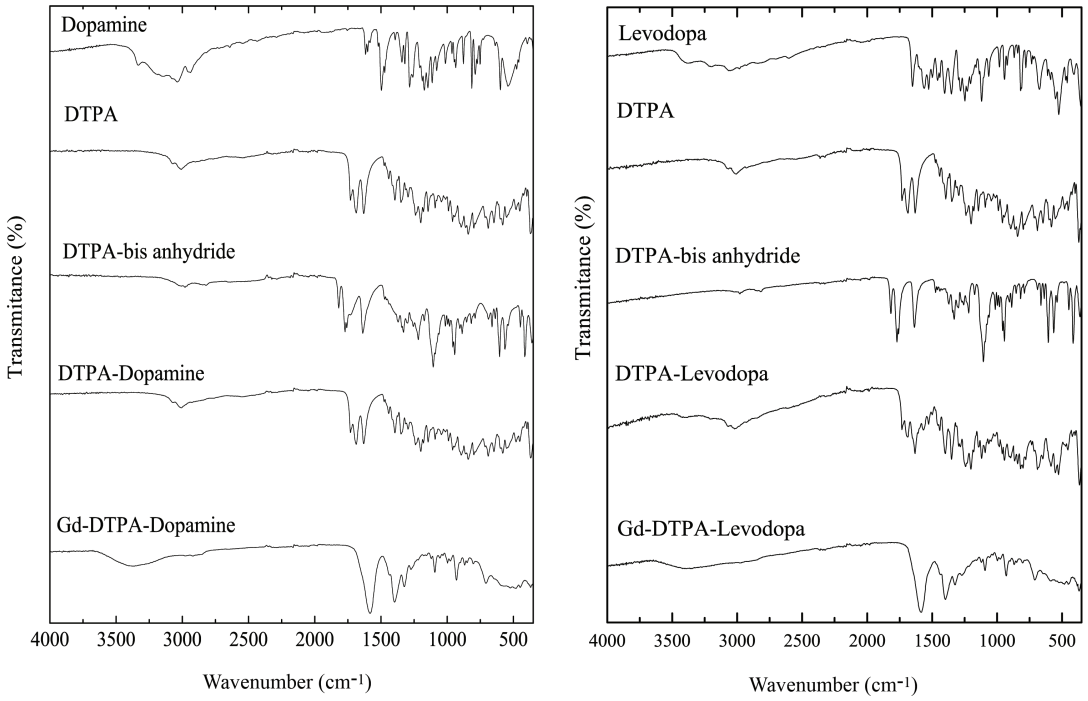

Figure 19 – Infrared Spectra of DTPA derivatives and Gadolinium complexes.

correspond to the stretching vibrations (ν) of the C=O link characteristic of the carboxylic group (present at 1630 cm^{-1} in DTPA, DTPA-bis anhydride and DTPA-Dopamine) and the monomer C=O (present at 1730 cm^{-1} in DTPA and

DTPA-Dopamine). After the complexation with Gadolinium, these bands disappear and a new band appears around 1580 cm^{-1}, which is denominated amides II, and is considered the fingerprint of an amide (-$CONH_2$) containing compound [82].

Levodopa derivatives of DTPA and the corresponding Gadolinium complex are presented on the right part of Figure 19. Similarly with the Dopamine derivatives, the Levodopa ones present the same vibrational bands proving that the linkage between Dopamine and DTPA is the same as Levodopa with DTPA, and that during the complexation to Gadolinium, an amide link is created [82].

Magnetic properties

During the phase exchange procedure, it was noticeable that only the Fe_3O_4 coated with Gd-DTPA-bislevodopa complex resulted in stable ferrofluids. Following this, the Gd-DTPA-bislevodopa complex was evaluated in terms of magnetic properties, namely magnetic susceptibility. Figure 20 shows the magnetic susceptibility of the Gd-DTPA-bislevodopa complex as a function of temperature and its Curie law adjust. From this

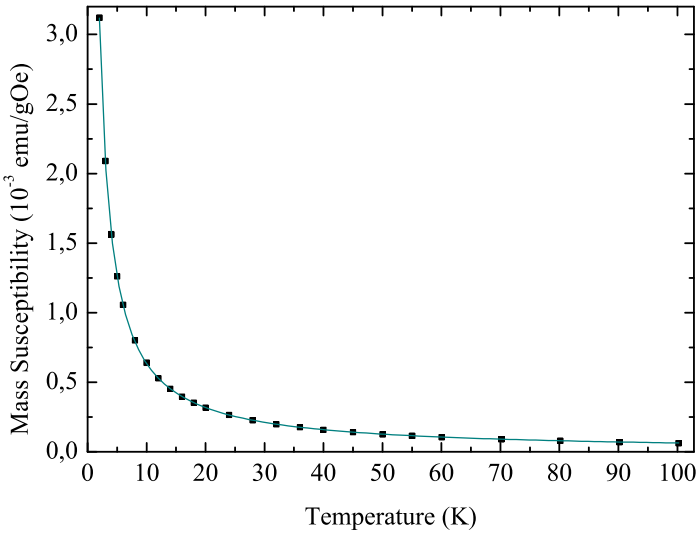

Figure 20 – Temperature dependence of susceptibility and Curie law adjust.

data, it is possible to calculate the relative amount of Gd^{3+} ions, using the Curie law:

$$\chi = \frac{C}{T} = n\,\frac{(g\,\mu_B)^2\;s\,(s+1)}{3\,k_B\,T} \tag{3.1}$$

where n is the number of Gd^{3+} ions per unit of mass. From this adjust, C can be determined. Since almost all the parameters of the equation are constants, and assuming

$s = \frac{7}{2}$, it is possible to estimate n. The calculated value for n using the Curie law adjust was 4.87×10^{20} Gd^{3+} ions per gram, which is similar to the "theoretical" value (calculated using the molecular mass of the compound) 6.6×10^{20} Gd^{3+} ions per gram. It is noticeable that the calculated value using the Curie law adjust is smaller than the "theoretical" one. This means that there are only approximately 74 % of the expected Gd^{3+} ions in the sample.

3.2.2 T_2 contrast agents

Fe_3Se_4 nanoparticles

As mentioned before Fe_3Se_4 nanoparticles are considered hard magnets and have a magnetic phase transition slightly above room temperature, which also makes them interesting to use as contrast agents. In fact, since these particles change their magnetic behaviour according to temperature, the MRI signal is also thought to change and so these particles can act as thermometers, using image contrast to define which zones of the body are warmer than usual.

The synthesis of Fe_3Se_4 nanoparticles is described in Chapter 2: Synthesis and Characterization, and the magnetic studies were presented and discussed in the previous section. MRI studies of Fe_3Se_4 nanoparticles were performed, and values of T_1 and T_2 were collected as a function of temperature (Figure 21). From top to bottom, the first pannels shows the R_1 and R_2values of Fe_3Se_4 nanoparticles as a function of temperature.

Roch et al [83] proposed a heuristic model, where R_1 and R_2 are expressed as the sum of two contributions (corresponding to the low and high anisotropy limits). For relatively low fields and high temperatures, the approximation $\frac{\mu B}{k_B T}1$, the most relevant terms are the pre-factors C_1 and C_2 given by 3.2:

$$C_1 = \left(\frac{32\pi}{135.000}\right)\gamma_H^2\mu_{SP}^2\left(\frac{N_S P}{RD}\right) = \frac{32}{16}C_2 \tag{3.2}$$

Where μ is the magnetic moment of the nanoparticles, N the nanoparticles density, R their radius and D the diffusion coefficient. Concerning the themperature dependence around the Curie temperature, the most relevant term is μ^2(T), which in turn is proportional to χT [84]. So, it is expected to see a similar temperature dependence on R_1, R_2 and χT curves. Indeed, the R_2 plot presents a similar shape to the χT plot. Although these results show to be promising, this part of the thesis requires further studies.

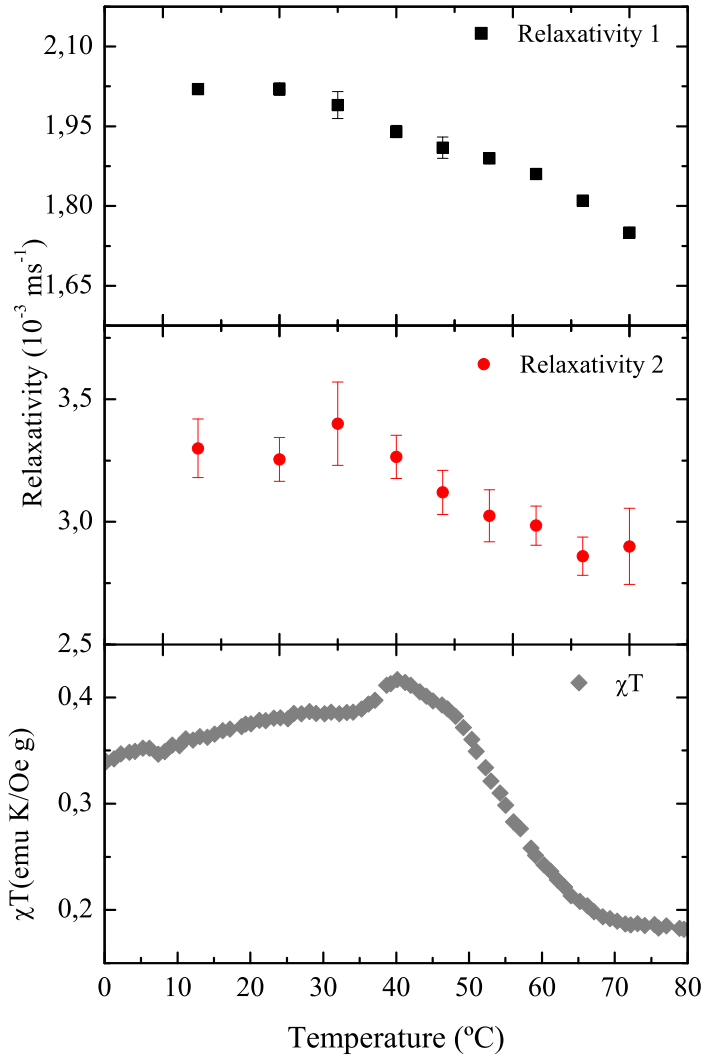

Figure 21 – MRI measures of Fe_3Se_4 nanoparticles at 7,2 MHz.

3.2.3 Dual-mode contrast agents

As mentioned before, the strategy for the synthesis of dual-mode contrast agents was to combine catecholamines, dopamine and levodopa, to link both to Gd-DTPA complexes (using the amine group) and the nanoparticles (using the hydroxyl group). The result of this combination was only successful for levodopa, yielding stable water-based ferrofluids.

One step Phase Exchange + Functionalization

10 mg of nanoparticles were dispersed in 50 mL of ethanol in an ultrasonic bath. Later, 624 mg of the Gadolinium complex were added and the mixture was left stirring under Nitrogen at 50 °C for 3 hours. The resulted mixture was then cooled and collected. The

functionalized nanoparticles were collected, centrifuged, and then dried in a fume hood. After the addition of 2 mL of water and a few minutes of dispersion inside an ultrasonic bath, the particles appeared to be stable in water.

This procedure was performed with different ratios of nanoparticle/complex, but only proved to be successful for the Gd-DTPA-bis levodopa complex.

Zeta Potential was performed in order to evaluate the charge signal at the surface of the nanoparticles coated with Gd-DTPA-bis levodopa, and the average result obtained was -22.83 mV, which is consistent to the results obtained previously with nanoparticles with levodopa coatings, showing that the carboxylic groups (-COOH) are left available at the surface of nanoparticles.

Infrared Spectroscopy

The Infrared spectra of Fe_3O_4 nanoparticles coated with the Gd-DTPA-Levo complex is presented in Figure 22, where the main band is situated at 1580 cm^{-1} and corresponds to the typical Amides II band [82].

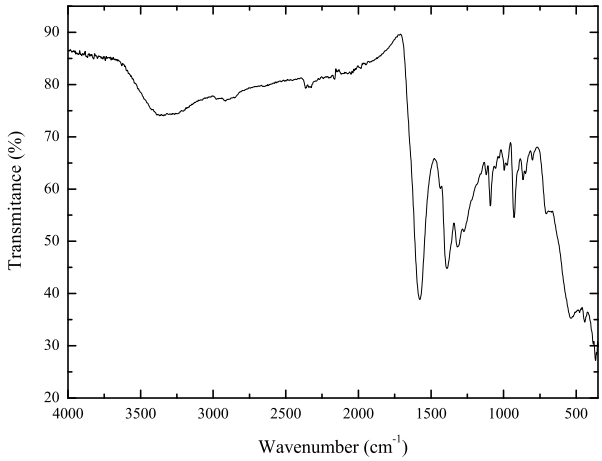

Figure 22 – Infrared Spectra of Fe_3O_4 nanoparticles functionalized with the Gd-DTPA-Levodopa complex.

During the timing of this thesis it was not possible to evaluate these nanomaterials for its capacity of being used as contrast agents, in order to conclude this work. Although, this is one of the tasks to be completed during the next few months.

4. Biological Evaluation

Due to the increased production of nanoparticles, it is important to know the effects of these materials in aquatic environments and their interaction with aquatic living species[1]. Regarding this, the first part of this Chapter starts by presenting an ecotoxicological evaluation of the nanoparticles, mainly the effects of these nanoparticles in *Xenopus laevis* tadpoles, used as model organisms. This ecotoxicological evaluation was conducted by Pedro Nunes, a Master student supervised by Dr. Isabela Lopes that collaborated with this thesis and will soon present his own.

The second part of this Chapter focuses on the effects of these materials in living cells, which is important when developing materials for biomedical applications. Thus, it is presented a cytotoxic evaluation of Fe_3Se_4 nanoparticles coated with dopamine in prostate cancer cells, which was performed by Dr. Vítor Gaspar.

4.1 *In Vivo* ecotoxicological evaluation

The African clawed frog (*Xenopus laevis*) is an amphibian model and widely employed for studies on genomics, endocrinology, toxicology and developmental biology. *Xenopus laevis* is an anuran amphibian from the *Pipidae* family, which originated in the African continent, where it appeared in several countries such as Angola, Cameroons, Congo, Zambia, among others. This species was considered invasive while being introduced in European countries, such as Portugal, France and the United Kingdom [85]. Nowadays this species is actually thriving, often increasing, as it has high reproductive potential, posing serious problems to some native species. A brief taxonomy of *Xenopus laevis* is presented in Table 5 [85].

Xenopus laevis has many advantages as a model organism, such as: (1) an easy regulation of reproduction; (2) the anaesthesia is accomplished by immerging in a narcotic solution;

[1]Unfortunately, the majority of residues from industry is still being sent to aquatic environments. Although this is a huge environmental problem, it is not discussed in the scope of this thesis, only acknowledged.

Table 5 – *Xenopus laevis* Taxonomy

Kingdom	Animalia
Phylum	Chordata
Class	Amphibia
Order	Anura
Family	Pipidae
Genus	*Xenopus*
Species	*Xenopus laevis*

(3) the organism is docile, harmless and easy to handle, thus accidental injury to the researcher can be avoided and (4) the organism can be kept easily and inexpensively [86].

Species maintenance

Adult organisms were maintained in glass aquariums. The room temperature was kept at 23 °C and the light availability was regulated to achieve 16 hours of light and 8 hours of obscurity, simulating a regular outdoor day. The population of adult organisms included 10 males and 32 females, which allowed the possibility of 320 different couples for reproduction purposes (organisms were chosen randomly concerning genetic variability).

The tadpoles (Figure 23) were kept in the same room conditions as the adults, but in smaller plastic recipients containing FETAX[2] medium, until used in any assay or died naturally. They were fed with common fish food (TetraMin^{TM} from Tetra^{TM}) every other day. The whole experimental procedure was performed recurring to *Xenopus laevis* tadpoles rather than adult organisms, due to ethical concerns, namely animal experimentation issues.

Figure 23 – *Xenopus laevis* tadpole.

[2]FETAX is a water-based culture medium containing different salts - such as $CaCl_2$, $CaSO_4$, KCl, $MgSO_4$, NaCl and $NaHCO_3$ - that is commonly stored within a pH range of 8±0.03 at room temperature.

Reproduction and egg harvesting

Eggs of the model organism were obtained by inducing egg laying *via* commercial Human Chorionic Gonadotropin (HCG) dorsal lymph sac injection, 12 to 16 hours prior to the desirable egg laying moment. The injected animals were subjected to a recovery time of 24 hours in the dark, before being returned into their aquariums, to prevent possible extra egg laying events occurring while in their captivities. This organisms need about 3 months of resting before being submitted to the same procedure, which makes them capable of doing so 4 times a year.

Toxicological Assays

The design of the assay consisted of 5 tadpoles in clear glass containers with 300 mL of a dispersion of nanoparticles in FETAX[3], for different concentrations and a control group with 4 replications each. The organisms were maintained at 23 °C along 16 hours of light and 8 hours of dark, checked every 24 hours - where endpoints were registered and the dead organisms were removed to prevent bacterial contaminations and consequently influencing the results.

Fe_3O_4 and Fe_3Se_4 nanoparticles were evaluated with dopamine and levodopa coatings. It was not possible yet to evaluate the surface functionalization with the Gadolinium complexes described in Chapter 3: Applications, due to the timing of this thesis. Assays to evaluate the effect of the nanoparticles without surface coatings were not possible to perform due to the impossibility of dispersing hydrophobic nanoparticles in FETAX.

Previous studies have been conducted to evaluate *in vivo* toxicological effects of Fe_3O_4 nanoparticles with different coatings. Results show that Fe_3O_4 nanoparticles do not have significant toxic effects, demonstrating good biocompatibility [87, 88].

Results and Discussion

The ecotoxicological evaluation is still in the beginning, so the results presented here are merely preliminary and should serve as a base to built upon for future reference. It is very clear that these results are in no way prepared for a publication, and further assays and biomarker studies need to be performed.

[3] In order to maintain a similar environment for the organisms, nanoparticles were dispersed directly on FETAX so that only these would be considered as invaders.

Fe_3O_4 @ Dopamine

Figure 24 shows the average cumulative mortality of *Xenopus laevis* tadpoles exposed to different concentrations of Fe_3O_4 nanoparticles functionalized with dopamine (Fe_3O_4 @ Dopamine) during 72 hours. Comparing the mortality values of the control population with the ones of tadpoles submitted to the presence of nanoparticles, the results appear to be similar. At lower concentrations, from 46.2 to 55.5 mg/L the particles seem to have no effect on the mortality of these organisms. With concentrations above 66 mg/L, the results indicate that these nanoparticles can, in fact, induce death or mobility problems that can later lead to death.

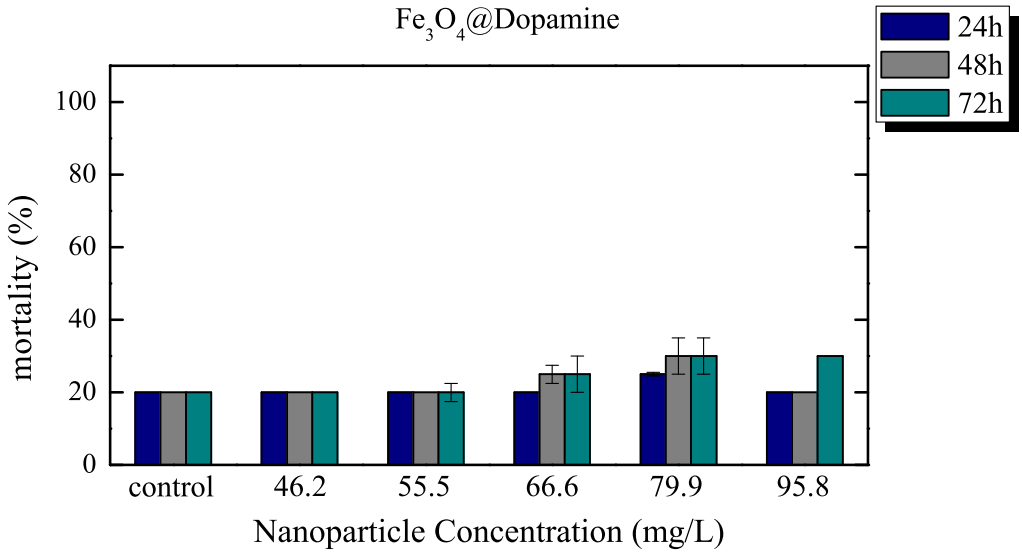

Figure 24 – Average cumulative mortality of *Xenopus laevis* tadpoles exposed during 72 hours to a series of concentrations of Fe_3O_4 @ Dopamine nanoparticles. Error bars represent standard deviation.

Fe_3O_4 @ Levodopa

Figure 25 shows the average cumulative mortality of *Xenopus laevis* tadpoles exposed to different concentrations of Fe_3O_4 nanoparticles functionalized with Levodopa (Fe_3O_4 @ Levodopa) during 72 hours. Fe_3O_4 @ Levodopa nanoparticles appear to affect the organisms more than what it was noticed in Fe_3O_4 @ Dopamine nanoparticles - although, at this point, these differences cannot be discussed due to lack of information. Figure 26 shows images of *Xenopus laevis* tadpoles while in the presence of Fe_3O_4 @ Levodopa nanoparticles.

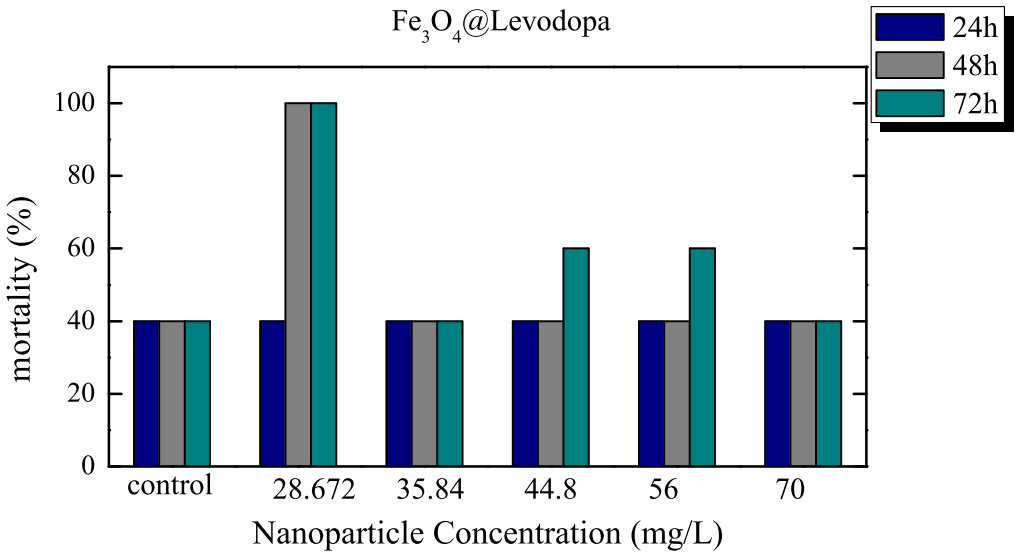

Figure 25 – Average cumulative mortality of *Xenopus laevis* tadpoles exposed during 72 hours to a series of concentrations of Fe_3O_4 @ Levodopa nanoparticles.

Figure 26 – *Xenopus laevis* in the presence of Fe_3O_4 @ Levodopa nanoparticles

Fe_3Se_4 @ Dopamine

Figure 27 shows the average cumulative mortality of *Xenopus laevis* tadpoles exposed to different concentrations of Fe_3Se_4 nanoparticles functionalized with dopamine (Fe_3Se_4 @ Dopamine) during 72 hours. In the presence of these nanoparticles, even at small concentrations (1.953 mg/L), the mortality seems to be superior after 72 hours than after 24 hours. This shows that the nanoparticles tend to have an over time accumulation effect, not an immediate one. Figure 28 shows images of *Xenopus laevis* tadpoles while in the presence of Fe_3Se_4 @ Dopamine nanoparticles.

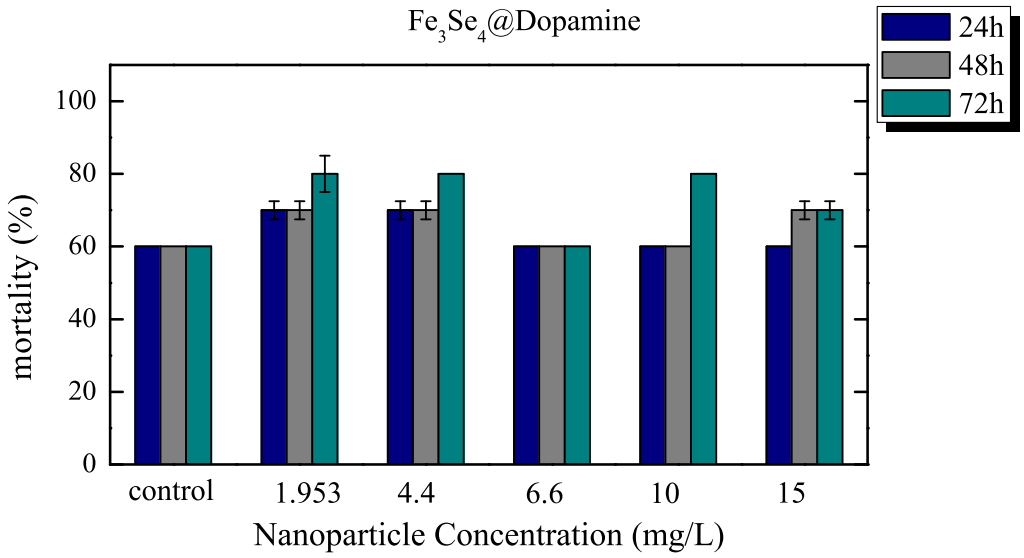

Figure 27 – Average cumulative mortality of *Xenopus laevis* tadpoles exposed during 72 hours to a series of concentrations of Fe_3Se_4 @ Dopamine nanoparticles. Error bars represent standard deviation.

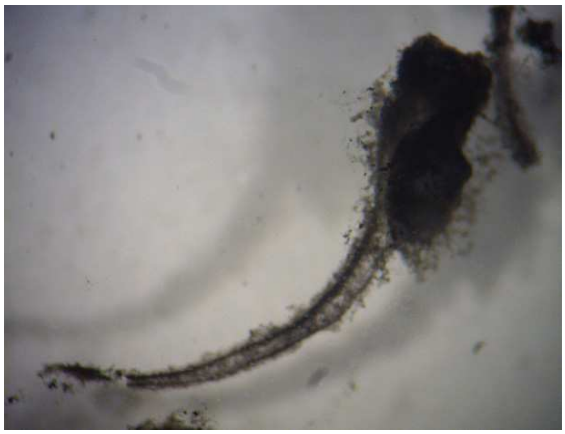

Figure 28 – *Xenopus laevis* tadpoles in the presence of Fe_3Se_4 @ Dopamine nanoparticles

Fe_3Se_4 @ Levodopa

Figure 29 shows the average cumulative mortality of *Xenopus laevis* tadpoles exposed to different concentrations of Fe_3Se_4 nanoparticles functionalized with levodopa (Fe_3Se_4 @ Levodopa). It is noticeable that Fe_3Se_4 nanoparticles can induce death in smaller concentrations than Fe_3O_4 nanoparticles. Also, these nanoparticles seem to have an effect over time, once the average mortality tends to increase over time. In the majority of analysed concentrations (above 4.4 mg/L), the mortality values reached 80-90%.

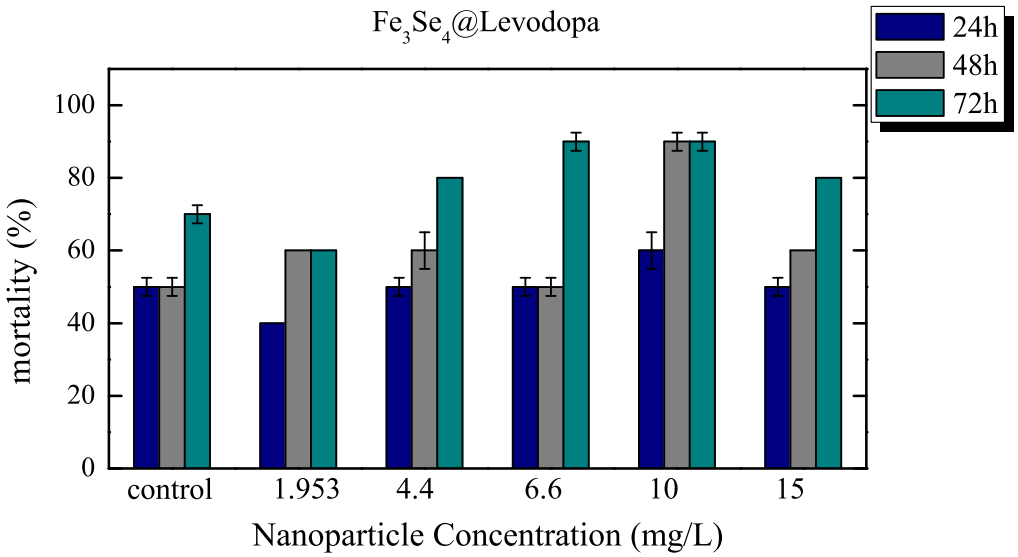

Figure 29 – Average cumulative mortality of *Xenopus laevis* tadpoles exposed during 72 hours to a series of concentrations of Fe_3Se_4 @ Levodopa nanoparticles. Error bars represent standard deviation.

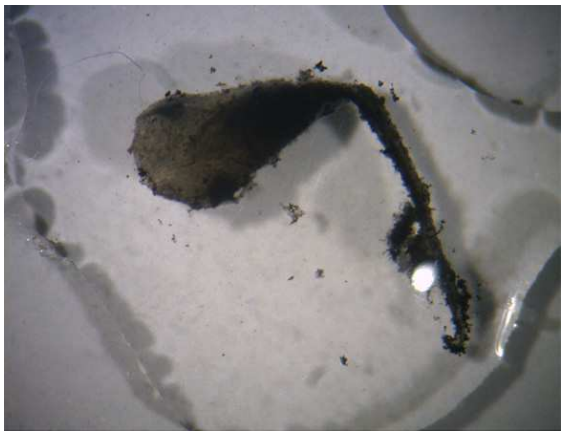

Figure 30 – *Xenopus laevis* tadpoles in the presence of Fe_3Se_4 @ Levodopa nanoparticles

During the observations of these assays, it was noticed that the nanoparticles tend to aggregate around the tadpole and link onto its skin. This often occurs in Fe_3Se_4 nanoparticles (as seen in Figures 28 and 30), which can be due to its larger size (>300 nm), when compared to Fe_3O_4 (<20 nm). The aggregation around the tadpoles often leads to induced malformations and moving difficulties, which can also explain why Fe_3Se_4 nanoparticles increases mortality at smaller doses. The coating of the nanoparticles was also a differentiation factor: the levodopa coated nanoparticles appear to increase mortality at smaller doses when compared to dopamine coated nanoparticles.

These studies will be continued, in the scope of the student's thesis, and other species will be evaluated in order to obtain clearer results.

4.2 *In Vitro* cytotoxic evaluation

Dopamine coated Fe_3Se_4 nanoparticles *in vitro* cytotoxicity was evaluated in 2D cultures of prostate cancer cells grown in complete cell culture medium. For cytotoxicity assays cells were then sub-cultured in 96 well plates. After 24 hours, the culture medium was removed, and cells were incubated with different nanoparticle concentrations in reduced medium for 4 hours. Afterwards, cell culture medium was removed, and cell viability was evaluated at 24 hours using the non-radioactive Alamar Blue® assay. For this purpose, cell were incubated with Alamar Blue® reagent for 4 hours. The fluorescence of the resulting resorufin was measured at an excitation/emission of λ_{ex} = 540 nm / λ_{em} = 600 nm by using a multi-mode microplate reader equipped with a tungsten halogen lamp.

Nanoparticle incubated cells were imaged after 24 hours following incubation by using an optical contrast microscope. As shown in Figure 31, Fe_3Se_4 nanoparticles do not elicit a cytotoxic response in PC-3 cells, however it is important to emphasize that nanoparticles precipitate in culture medium. Hence the cytotoxicity data obtained by Alamar Blue® assays should be carefully evaluated since the nanoparticles may have not entered PC-3 cells. The fact that the nanoparticles aggregated around the cells may be interesting for cell-binding applications. Furthermore, in order to design the nanoparticles for internalizing their surfaces should be modified, for example, with proteins.

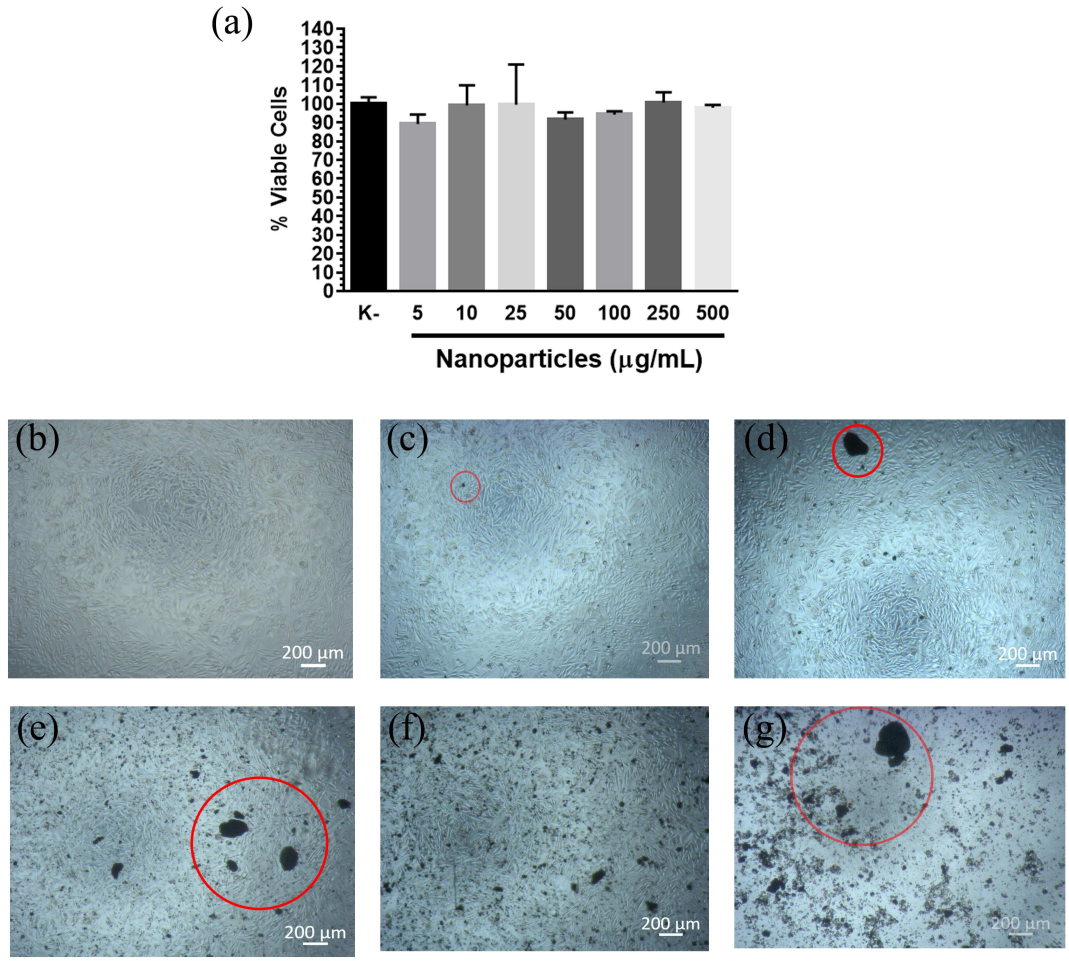

Figure 31 – **Fe_3Se_4 nanoparticles cytotoxicity characterization.** **(a)** Alamar blue® analysis of PC-3 cells viability upon incubation with Fe_3Se_4 nanoparticles. Data is represented as mean ± s.d. (n =5). K- represents PC-3 cells non-incubated. Optical contrast micrographs of PC-3 cells: **(b)** control, i.e., non-incubated with nanoparticles; **(c)** Fe_3Se_4 nanoparticles 5 μg/mL; **(d)** Fe_3Se_4 nanoparticles 10 μg/mL; **(e)** Fe_3Se_4 nanoparticles 100 μg/mL; **(f)** Fe_3Se_4 nanoparticles 250 μg/mL; **(g)** Fe_3Se_4 nanoparticles 500 μg/mL;

5. Conclusions and Outlook

In the beginning, this thesis was focused on the development of magnetic nanoparticles to act as contrast agents for MRI. In order to achieve this, Fe_3O_4 and Fe_3Se_4 nanoparticles were synthesized and characterized. The development included the synthesis, characterization and the surface coating procedures that were specially developed to achieve a phase exchange and a functionalization in just one step. The synthesis of Fe_3O_4 nanoparticles is widely studied and used by scientists all over the world. Still, the one step phase exchange and surface functionalization methods here reported represent a simplified green surface coating procedure, which may be used in several biomedical applications, specially ones that require small surface coatings. On the other hand, the synthesis of Fe_3Se_4 nanoparticles here presented appears to be one of pioneer methods for this specific inorganic phase. In fact, it took approximately 2 years to improve the synthesis methods of Fe_3Se_4 nanoparticles, and there are still details to be perfected.

At a certain point came the idea of using Fe_3Se_4 nanoparticles as logic gates that respond to temperature and magnetic field as inputs, due to its T_C slightly above room temperature. Given the collaboration with Dr. Vítor Gaspar and Professor João Mano, it was possible to evaluate the behaviour of Fe_3Se_4 nanoparticles in hyperthermia cellular assays, which proved to be successful in determining whether or not the cells were heated up above 40 °C.

During this time, and regarding the MRI application, Gadolinium-based metal-organic complexes, with dopamine and levodopa, were developed in order to further be used as a surface coating for Fe_3O_4 nanoparticles. Although the metal-organic synthesis were achieved successfully, the surface functionalization of nanoparticles only worked for Gadolinium DTPA-bislevodopa. There is no current explanation for this, but hopefully this obstacle will be overcome and the Gadolinium DTPA-bisdopamine will soon be anchored onto the surface of Fe_3O_4 nanoparticles.

The *in vivo* ecotoxicological evaluation was performed in collaboration with Pedro Nunes, a Master student supervised by Dr. Isabel Lopes from the University of Aveiro. The majority of replicas showed that the nanoparticles tend to aggregate in the biological medium and around the organisms, leading them to develop malfunctions and disturb their typical movement. For now, this study is not deeply explored, but hopefully will soon answer some questions about the interaction between the nanoparticles and its effects on living beings.

The *in vitro* cytotoxic evaluation was performed in collaboration with Dr. Vítor Gaspar. This study agrees with the previous one, as the observations show that the majority of the nanoparticles tend to aggregate in biological mediums and link onto the surface of cells and living beings.

There is still room to grow, as always. With that in mind, the planned future work includes:

- The use of Fe_3O_4 nanoparticles mixed with Fe_3Se_4 nanoparticles in order to Fe_3O_4 nanoparticles act as heat sources, and Fe_3Se_4 nanoparticles act as thermometers.
- The preparation of dual-mode contrast agents with a variety of known concentrations in order to evaluate the NMR signal according to concentration of contrast agents.
- The *in vivo* ecotoxicological evaluation studies are still currently being developed, and there are several tasks to do regarding this topic. As of this moment, studies on *P. perezi*, the most common amphibian in Portugal, are being conducted. These studies are specially important for nanoparticles that can later be used as contrast agents, i.e. need to enter the organism and still be harmless.
- Several sub-cellular parameters will be tested, using the evaluation of two types of biological biomarkers. These markers can be considered as main endpoints on toxicity effects.
- The *in vivo* ecotoxicological evaluation of the prepared Gadolinium complexes and its combination with Fe_3O_4 nanoparticles, as well as the evaluation of the effects of Dopamine and Levodopa without the presence of nanoparticles.
- The *in vitro* cytotoxic evaluation are currently being developed in order to have a complete analysis of all the nanoparticles and surfaces.

In summary, this thesis led to the development of what can be considered parallel research projects, all of them including the development and functionalization of

magnetic nanoparticles. As a personal opinion, this thesis lifts the veil on several questions regarding the development of different dual-mode contrast agents, and the advance on temperature control on hyperthermia assays. With that in mind, this thesis will hopefully be used as a starting platform giving rise to new projects.

Bibliography

[1] C. Bréchignac, P. Houdy, and M. Lahmani. *Nanoscience: Nanomaterials and Nanochemistry*. Springer, 2007.

[2] D. Schaming and H. Remita. Nanotechnology: from the ancient time to nowadays. *Foundations of Chemistry*, 17:187–205, 2015.

[3] P. Guardia, A. Labarta, and X. Batlle. Tuning the size, the shape, and the magnetic properties of iron oxide nanoparticles. *The Journal of Physical Chemistry C*, 115(2):390–396, 2011.

[4] C. Kumar. *Nanomaterials for Biosensors*, volume 8 of *Nanotechnologies for the Life Sciences*. Wiley-VCH, 2007.

[5] E. V. Dirote. *Nanotechnology at the Leading Edge*. Nova Science Publisher, 2006.

[6] A. Jebnd F. H. E. Hajjar, S. Hekmatimoghaddam, B. Kazemi, J. M. de la Fuente, and M. Rashidi. Triangular gold nanoparticles conjugated with peptide ligands: A new class of inhibitor for *Candida albicans* secreted aspartyl poteinase. *Biochemical Pharmacology*, 90:349–355, 2014.

[7] T. Trindade and P.J. Thomas. Defining and using very small crystals. In *Comprehensive Inorganic Chemistry*, pages 343–369. Elsevier, Amsterdam, 2nd edition, 2013.

[8] J. Koch and R. Sabirianov. Finite size effects in shell nanoparticles. *Journal of Magnetism and Magnetic Materials*, 321(9):1137 – 1141, 2009.

[9] X. Liu, P. K. Chu, and C. Ding. Surface nano-functionalization of biomaterials. *Materials Science and Engineering: Reports*, 70(3):275–302, 2010.

[10] Z. Hedayatnasab, F. Abnisa, and W. M. A. W. Daud. Review on magnetic nanoparticles for magnetic nanofluid hyperthermia application. *Materials and Design*, 123:174 – 196, 2017.

[11] H. E. Çamurlu, S. Mathur, O. Arslan, and E. Akarsu. Modification of hexagonal boron nitride nanoparticles with fluorosilane. *Ceramics International*, 42:6312–6318, 2016.

[12] R. Oliveira-Silva, J. P. da Costa, R. Vitorino, and A. L. Daniel da Silva. Magnetic chelating nanoprobes for enrichment and selective recovery of metalloproteases from human saliva. *Journal of Materials Chemistry B*, 3:238–249, 2015.

[13] J. Park, K. An, Y. Hwang, J. Park, H. Noh, J. Kim, J. Park, N. Hwang, and T. Hyeon. Ultra-large-scale syntheses of monodisperse nanocrystals. *Nature Materials*, 3:891–895, 2004.

[14] L. M. Bronstein, X. Huang, J. Retrum, A. Schmucker, M. Pink, B. D. Stein, and B. Dragnea. Influence of iron oleate complex structure on iron oxide nanoparticle formation. *Chemistry of Materials*, 19(15):3624–3632, 2007.

[15] N. Lee, Y. Choi, Y. Lee, M. Park, W. K. Moon, S. H. Choi, and T. Hyeon. Water-dispersible ferrimagnetic iron oxide nanocubes with extremely high R_2 relaxivity for highly sensitive *in vivo* MRI of tumors. *Nano Letters*, 12(6):3127–3131, 2012.

[16] D. Kim, N. Lee, M. Park, B. H. Kim, K. An, and T. Hyeon. Synthesis of uniform ferrimagnetic magnetite nanocubes. *Journal of the American Chemical Society*, 131(2):454–455, 2009.

[17] P. Guardia, N. Pérez, A. Labarta, and X. Batlle. Controlled synthesis of iron oxide nanoparticles over a wide size range. *Langmuir*, 26(8), 2010.

[18] D. Aluani, V. Tzankova, M. Kondeva-Burdina, Y. Yordanov, E. Nikolova, F. Odzhakov, A. Apostolov, T. Markova, and K. Yoncheva. Evaluation of biocompatibility and antioxidant efficiency of chitosan-alginate nanoparticles loaded with quercetin. *International Journal of Biological Macromolecules*, 103:771–782, 2017.

[19] J. van Embden, A. S. R. Chesman, and J. J. Jasieniak. The heat-up synthesis of colloidal nanocrystals. *Chemistry of Materials*, 27:2246–2285, 2015.

[20] J. W. M. Bulte and M. M. J. Modo. *Nanoparticles in Biomedical Imaging*, volume 3 of *Fundamental Biomedical Technologies*. Springer, 2007.

[21] K. Chatterjee, S. Sarkar, K. J. Rao, and S. Paria. Core/shell nanoparticles in biomedical applications. *Advances in Colloid and Interface Science*, 209:8–39, 2014.

[22] A. Tavakoli, M. Sohrabi, and A. Kargari. A review of methods for synthesis of nanostructured metals with emphasis on iron compounds. *Chemical Papers*, 61(3):151–170, 2007.

[23] A. Ali, H. Zafar, M. Zia, I. ul Haq, A. R. Phull, J. S. Ali, and A. Hussain. Synthesis, characterization, applications, and challenges of iron oxide nanoparticles. *Nanotechnology, Science and Applications*, 6(9):49–67, 2016.

[24] J. Natsuki. A review of silver nanoparticles: Synthesis methods, properties and applications. *International Journal of Materials Science and Applications*, 4:325, 2015.

[25] H. R. Ghorbani. A review of methods for synthesis of Al nanoparticles. *Orient J Chem*, 30(4):941–1949, 2014.

[26] D. V. Talapin and E. V. Shevchenko. Introduction: Nanoparticle chemistry. *Chemical Reviews*, 116(18):10343–10345, 2016.

[27] S. Navalón and H. García. Nanoparticles for catalysis. *Nanomaterials*, 6:123–125, 2016.

[28] N. F. Santos, U. Zubets, A. F. Carvalho, A. J. S. Fernandes, L. Pereira, and F. M. Costa. Tuning the field emission of graphene-diamond hybrids by pulsed flow CVD. *Carbon*, 122:726–736, 2017.

[29] W. C. W. Chan. *Bio-applications of Nanoparticles*, volume 620 of *Advances in Experimental Medicine and Biology*. Landes Bioscience, 2007.

[30] B. D. Fellows, N. Ghobrial, E. Mappus, A. Hargett, M. Bolding, D. Dean, and O. T. Mefford. In vitro studies of heparin-coated magnetic nanoparticles for use in the treatment of neointimal hyperplasia. *Nanomedicine: Nanotechnology, Biology and Medicine*, 14(4):1191–1200, 2018.

[31] K. L. Kompa and R. D. Levine. A molecular logic gate. *Proceedings of the National Academy of Sciences*, 98(2):410–414, 2001.

[32] A. Saghatelian, N. H. Volcker, K. M. Guckian, V. S. Lin, and M. R. Ghadiri. DNA-based photonic logic gates+ AND, NAND, and INHIBIT. *Journal of the American Chemical Society*, 125(2):346–347, 2003.

[33] A. V. Orlov, A. Pushkarev, E. N. Mochalova, P. I. Nikitin, and M. P. Nikitin. Development and label-free investigation of logic-gating biolayers for smart biosensing. *Sensors and Actuators B: Chemical*, 257:971–979, 2018.

[34] J. Chen, Z. Fang, P. Lie, and L. Zeng. Computational lateral flow biosensor for proteins and small molecules: A new class of strip logic gates. *Analytical Chemistry*, 84(15):6321–6325, 2012.

[35] X. Yu, W. Lian, J. Zhang, and H. Liu. Multi-input and -output logic circuits based on bioelectrocatalysis with horseradish peroxidase and glucose oxidase immobilized in multi-responsive copolymer films on electrodes. *Biosensors and Bioelectronics*, 80:631–639, 2016.

[36] I. L. Sokolov, V. R. Cherkasov, A. A. Tregubov, S. R. Buiucli, and M. P. Nikitin. Smart materials on the way to theranostic nanorobots: Molecular machines and nanomotors, advanced biosensors, and intelligent vehicles for drug delivery. *Biochimica et Biophysica Acta - General Subjects*, 1861(6):1530–1544, 2017.

[37] Y. Lai, S. Sun, and M. Chuang. Biosensors with built-in biomolecular logic gates for practical applications. *Biosensors (Basel)*, 4(3):273–300, Sep 2014.

[38] H. Grebel. Logic gates with ion transistors. *Thin Solid Films*, 638:138–143, 2017.

[39] P. Wilson. Latches, flip-flops, and registers. In *Design Recipes for FPGAs*, chapter 20, pages 285–294. Newnes, second edition edition, 2016.

[40] M. Mallory, E. Gogineni, G. C. Jones, L. Greer, and C. B. Simone II. Therapeutic hyperthermia: The old, the new, and the upcoming. *Critical Reviews in Oncology/Hematology*, 97:56–64, 2016.

[41] A. Sohail, Z. Ahmad, O. Anwar Bég, Sa. Arshad, and L. Sherin. A review on hyperthermia via nanoparticle-mediated therapy. *Bulletin du Cancer*, 104(5):452–461, 2017.

[42] N. R. Datta, S. Gómez Ordóñez, M. M. Paulides U. S. Gaipl, H. Crezee, D. Marder J. Gellermann, E. Puric, and S. Bodis. Local hyperthermia combined with radiotherapy and-/or chemotherapy: Recent advances and promises for the future. *Cancer Treatment Reviews*, 41(9):742–753, 2015.

[43] D. K. Chatterjee, P. Diagaradjane, and S. Krishnan. Nanoparticle-mediated hyperthermia in cancer therapy. *Therapeutic Delivery*, 2(8):1001–1014, Aug 2011.

[44] R. Piñol, C. D. S. Brites, R. Bustamante, A. Martínez, N. J. O. Silva, J. L. Murillo, R. Cases, J. Carrey, C. Estepa, C. Sosa, F. Palacio, L. D. Carlos, and A. Millán. Joining time-resolved thermometry and magnetic-induced heating in a

single nanoparticle unveils intriguing thermal properties. *ACS Nano*, 9(3):3134–3142, 2015.

[45] M. Y. M. Chen, T. L. Pope, and D. J. Ott. *Basic Radiology*, volume 2. McGraw Hill, 2011.

[46] D. W. McRobbie, E. A. Moore, M. J. Graves, and M. R. Prince. *MRI From Picture to Proton*, volume 2. Cambridge, 2006.

[47] H. Shokrollahi. Contrast agents for MRI. *Materials Science and Engineering C*, 33:4485–4497, 2013.

[48] P. Carretta and A. Lascialfari. *NMR-MRI, μSR and Mössbauer Spectroscopies in Molecular Magnets*. Springer Milan, 2007.

[49] S. A. Wickline E. A. Waters. Contrast agents for MRI. *Basic Research in Cardiology*, 103:114–121, 2008.

[50] Nanasaheb D. Thorat, Raghvendra A. Bohara, Hemraj M. Yadav, and Syed A. M. Tofail. Multi-modal MR imaging and magnetic hyperthermia study of Gd doped Fe_3O_4 nanoparticles for integrative cancer therapy. *RSC Advances*, 6, 2016.

[51] K. Chamé, M. Ojeda, F. González, O. Meza, L. Ojeda, and C. Velásquez. Synthesis and luminescent properties of multifunctional $Ag@Fe_3O_4@Gd_2O_3Eu^{3+}$ composite. *Journal of Alloys and Compounds*, 704(Supplement C):212 – 217, 2017.

[52] M. Yang, L. Gao, K. Liu, C. Luo, Y. Wang, L. Yu, H. Peng, and W. Zhang. Characterization of $Fe_3O_4/SiO_2/Gd_2O(CO_3)_2$ core/shell/shell nanoparticles as T_1 and T_2 dual mode mri contrast agent. *Talanta*, 131(Supplement C):661 – 665, 2015.

[53] L. Zhang, S. Liang, R. Liu, T. Yuan, S. Zhang, Z. Xu, and H. Xu. Facile preparation of multifunctional uniform magnetic microspheres for T_1-T_2 dual modal magnetic resonance and optical imaging. *Colloids and Surfaces B: Biointerfaces*, 144(Supplement C):344–354, 2016.

[54] W. Wu, Z. Wu, T. Yu, C. Jiang, and W. Kim. Recent progress on magnetic iron oxide nanoparticles: synthesis, surface functional strategies and biomedical applications. *Science and Technology of Advanced Materials*, 16(2):023501, 2015.

[55] W. Wu, Q. He, and C. Jiang. Magnetic iron oxide nanoparticles: Synthesis and surface functionalization strategies. *Nanoscale Research Letters*, 3(11):397–415, 2008.

[56] L. Yang, Z. Cao, H. K. Sajja, H. Mao, L. Wang, H. Geng, H. Xu, T. Jiang, W. C. Wood, S. Nie, and Y. A. Wang. Development of receptor targeted magnetic iron oxide nanoparticles for efficient drug delivery and tumor imaging. *Journal of Biomedical Nanotechnology*, 4(4):439–449, 2008.

[57] S. Laurent, S. Dutz, U. O. Häfeli, and M. Mahmoudi. Magnetic fluid hyperthermia: Focus on superparamagnetic iron oxide nanoparticles. *Advances in Colloid and Interface Science*, 166(1):8–23, 2011.

[58] M. Cao, Z. Li, J. Wang, W. Ge, T. Yue, R. Li, V. L. Colvin, and W. W. Yu. Food related applications of magnetic iron oxide nanoparticles: Enzyme immobilization, protein purification, and food analysis. *Trends in Food Science and Technology*, 27(1):47–56, 2012.

[59] N. Lee and T. Hyeon. Designed synthesis of uniformly sized iron oxide nanoparticles for efficient magnetic resonance imaging contrast agents. *Chemical Society Reviews*, 41:2575–2589, 2012.

[60] R. M. Cornell. *Electronic, Electrical and Magnetic Properties and Colour*, chapter 6, pages 111–137. Wiley-Blackwell, 2004.

[61] V. Pecharsky and P. Zavalij. *Fundamentals of Powder Diffraction and Structural Characterization of Materials*. Springer US, 2005.

[62] T. Yamanaka, H. Shimazu, and K. Ota. Electric conductivity of Fe_2SiO_4-Fe_3O_4 spinel solid solutions. *Physics and Chemistry of Minerals*, 28:110–118, 2001.

[63] B.C. Smith. *Fundamentals of Fourier Transform Infrared Spectroscopy, Second Edition*. CRC Press, 2011.

[64] H. Zhang, G. Long, D. Li, R. Sabirianov, and H. Zeng. Fe_3Se_4 nanostructures with giant coercivity synthesized by solution chemistry. *Chemistry of Materials*, 23(16):3769–3774, 2011.

[65] J. E. Dutrizac, M. B. I. Janjua, and J. M. Toguri. Phase studies on the iron–selenium system. *Canadian Journal of Chemistry*, 46(8):1171–1174, 1968.

[66] C. Bullen, J. van Embden, J. J. Jasieniak, J. E. Cosgriff, R. J. Mulder, E. Rizzardo, M. Gu, and C. L. Raston. High activity phosphine-free selenium precursor solution for semiconductor nanocrystal growth. *Chemistry of Materials*, 22(14):4135–4143, 2010.

[67] A.F. Andresen and R. van Laar. The magnetic structure of fe3se4. *Acta Chemica Scandinavica*, 24:2435–2439, 1970.

[68] R. M. Patil, N. D. Thorat, P. B. Shete, P. A. Bedge, S. Gavde, M. G. Joshi, S. A. M. Tofail, and R. A. Bohara. Comprehensive cytotoxicity studies of superparamagnetic iron oxide nanoparticles. *Biochem Biophys Rep*, 13:63–72, Mar 2018.

[69] E. D. Smolensky, H. E. Park, T. S. Berquó, and V. C. Pierre. Surface functionalization of magnetic iron oxide nanoparticles for mri applications – effect of anchoring group and ligand exchange protocol. *Contrast Media and Molecular Imaging*, 6(4):189–199.

[70] O. Zvarec, S. Purushotham, A. Masic, R. V. Ramanujan, and A. Miserez. Catechol-functionalized chitosan/iron oxide nanoparticle composite inspired by mussel thread coating and squid beak interfacial chemistry. *Langmuir*, 29(34):10899–10906, 2013.

[71] Y. Liu, T. Chen, C. Wu, L. Qiu, R. Hu, J. Li, S. Cansiz, L. Zhang, C. Cui, G. Zhu, M. You, T. Zhang, and W. Tan. Facile surface functionalization of hydrophobic magnetic nanoparticles. *Journal of the American Chemical Society*, 136(36):12552–12555, 2014.

[72] W. Wang, Y. Dai, H. Zhang, H. Luo, and Y. Chen. Preparation and characterization of superparamagnetic iron oxide nanoparticle-graphene oxide nanocomposites. *Journal of Nanoscience and Nanotechnology*, 16(7):7159–7163, 2016.

[73] N. Winterton. Green chemistry: deliverance or distraction? *Clean Technologies and Environmental Policy*, 18(4):991–1001, Apr 2016.

[74] N. Ndraha, H. Hsiao, J. Vlajic, M. Yang, and H. V. Lin. Time-temperature abuse in the food cold chain: Review of issues, challenges, and recommendations. *Food Control*, 89:12–21, 2018.

[75] K. Motoki, T. Saito, R. Nouchi, R. Kawashima, and M. Sugiura. The paradox of warmth: Ambient warm temperature decreases preference for savory foods. *Food Quality and Preference*, 69:1–9, 2018.

[76] M. Ebrahimi. On the temperature control in self-controlling hyperthermia therapy. *Journal of Magnetism and Magnetic Materials*, 416:134–140, 2016.

[77] A. Carattino, M. Caldarola, and M. Orrit. Gold nanoparticles as absolute nanothermometers. *Nano Letters*, 18(2):874–880, 2018.

[78] D. Gareau, A. Desrosiers, and A. Vallée-Bélisle. Programmable quantitative DNA nanothermometers. *Nano Letters*, 16(7):3976–3981.

[79] M. Getzlaff. *Magnetism in Reduced Dimensions - Nanoparticles*, chapter 12, pages 175–207. Springer, 2008.

[80] C.F.G.C. Geraldes, A.M. Urbano, M.C. Alpoim, A.D. Sherry, K. T. Kuan, R. Rajagopalan, F. Maton, and R. N. Muller. Preparation, physico-chemical characterization, and relaxometry studies of various Gadolinium(III)-DTPA-bis(amide) derivatives as potential magnetic resonance contrast agents. *Magnetic Resonance Imaging*, 13(3):401–402, 1995.

[81] X. Zhou, L. Yang, G. Yan, W. Xu, C. Zhou, Q. Zhang, L. Li, F. Liu, J. Guo, and Q. Zhao. Dopamine-containing gadolinium complex as magnetic resonance imaging contrast agent. *Journal of Rare Earths*, 30(9):884 – 889, 2012.

[82] T. N. Parac-Vogt, K. Kimpe, and K. Binnemans. Heterobimetallic Gadolinium(III)-iron(III) complex of DTPA-bis(3-hydroxytyramide). 374(1-2):325–329, 2004.

[83] A. Roch, R. N. Muller, and P. Gillis. Theory of proton relaxation induced by superparamagnetic particles. *The Journal of Chemical Physics*, 110(11):5403–5411, 1999.

[84] Amiri Houshang, Bustamante Rodney, Millán Angel, Silva Nuno J.O., Piñol Rafael, Gabilondo Lierni, Palacio Fernando, Arosio Paolo, Corti Maurizio, and Lascialfari Alessandro. Magnetic and relaxation properties of multifunctional polymer-based nanostructured bioferrofluids as mri contrast agents. *Magnetic Resonance in Medicine*, 66(6):1715–1721.

[85] Xenopus laevis (Daudin, 1802). Retrieved June, 27^{th}, 2018 from the Integrated Taxonomic Information System on-line database (http://www.itis.gov).

[86] C. Liu, X. Xia, L. Sun, X. Luan, Y. Jin, and L. Liu. Female hormone release of microencapsulated xenopus laevis ovarian cells. *International Journal of Pharmaceutics*, 450(1):177–184, 2013.

[87] F. Wang, X. Li, W. Li, H. Bai, Y. Gao, J. Ma, W. Liu, and G. Xi. Dextran coated fe3o4 nanoparticles as a Near-Infrared laser-driven photothermal agent for efficient ablation of cancer cells *in vitro* and *in vivo*. *Materials Science and Engineering: C*, 90:46–56, 2018.

[88] Q.L. Jiang, S.W. Zheng, R.Y. Hong, S.M. Deng, L. Guo, R.L. Hu, B. Gao, M. Huang, L.F. Cheng, G.H. Liu, and Y.Q. Wang. Folic acid-conjugated Fe_3O_4 magnetic nanoparticles for hyperthermia and MRI *in vitro* and *in vivo*. *Applied Surface Science*, 307:224–233, 2014.

A. Appendix

A.1 NMR

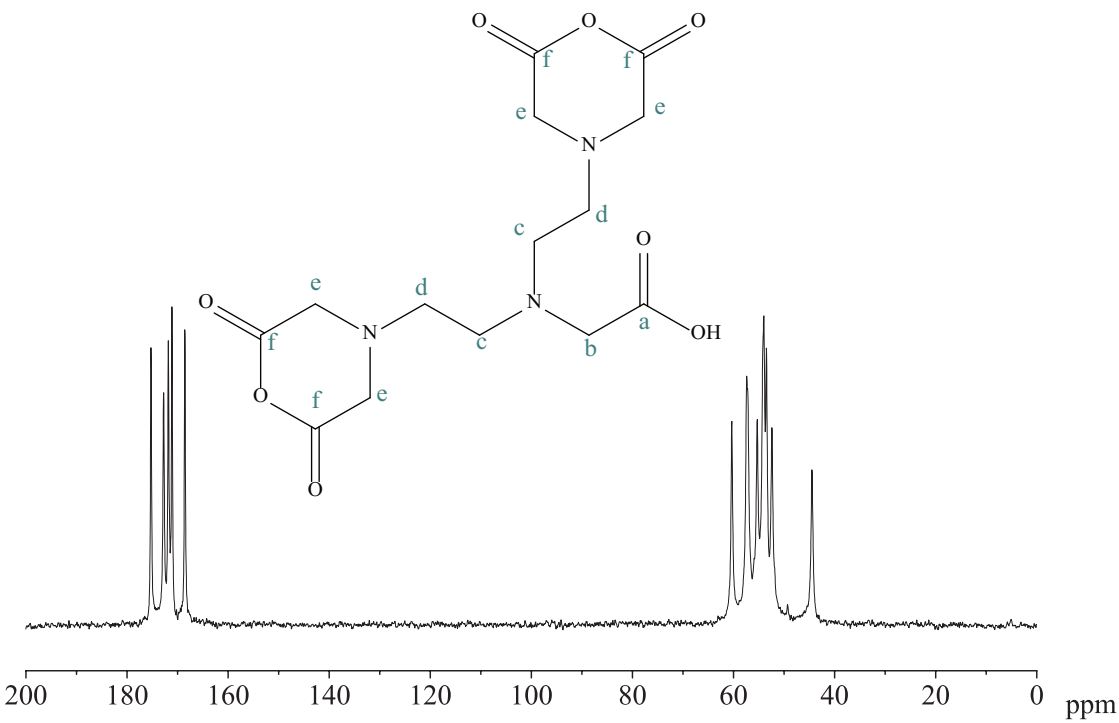

Figure A1 – Solid State ^{13}C NMR of DTPA bis anhydride.

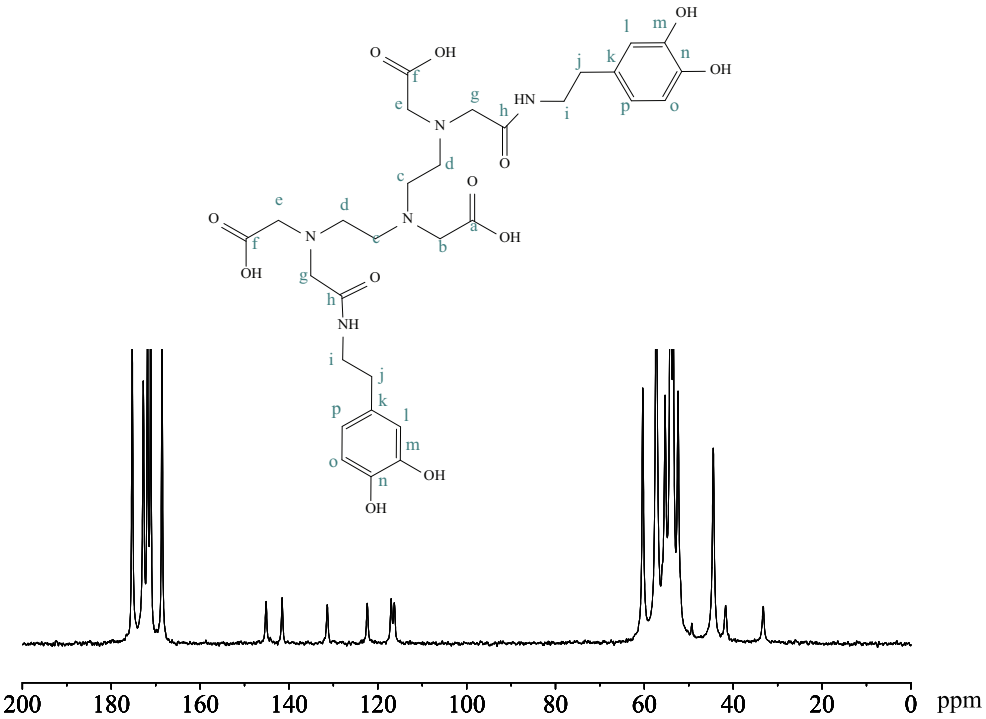

Figure A2 – Solid State ^{13}C NMR of DTPA bis dopamine.

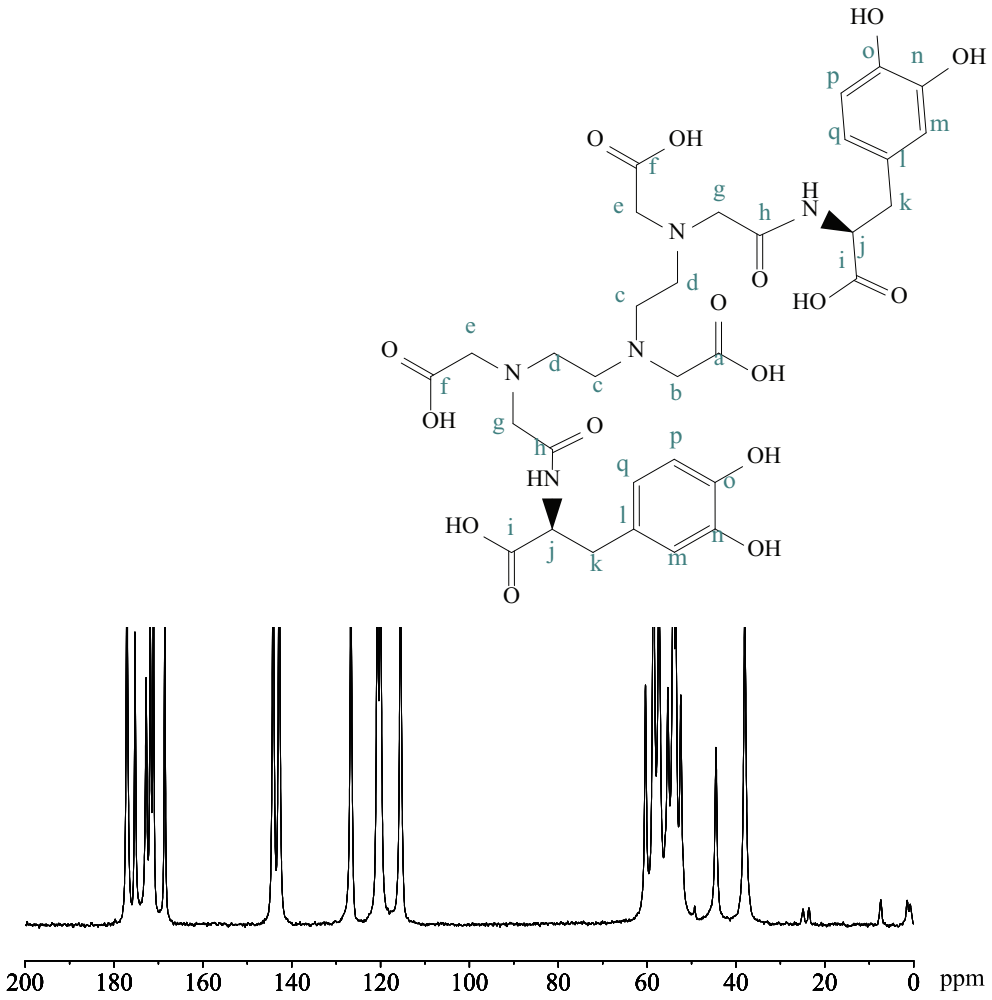

Figure A3 – Solid State ^{13}C NMR of DTPA bis levodopa.

A.2 Experimental

A.2.1 X-ray Diffraction

X-ray diffraction (XRD) measurements were performed at room temperature with a PANalytical Empyrean powder diffractometer using monochromated CuK$_\alpha$ radiation (λ = 1.541 °A) in the 10-100 °(2θ) range at 0.02 °resolution, and 4000 acquisition points per step. The incident beam optics included a Soller slit of 0.04 rad, a 10 mm fixed mask, a divergence fixed slit of 1/4 and an anti-scatter slit of 1/8. The diffracted beam optics included a Soller slit of 0.04 rad and anti-scatter slit of 7.5 mm. The analysis of the diffraction patterns was performed by Rietveld refinement using the FullProf package. The size effects were treated with the integral breadth method using the Voigt model

for both the instrumental and intrinsic diffraction peak shape considering a Thompson-Cox-Hastings pseudo-Voigt convoluted with Axial divergence asymmetry function to describe the peak shape. The contribution of the instrument to the peaks broadening was determined by the refinement of the XRD pattern of a LaB6 standard sample (NIST ref. 660a).

A.2.2 Infrared Spectroscopy

Infrared spectra (FTIR) were obtained in a FTIR Brucker Tensor 27 equipped with an OPUS® (V4.5) software, in the wavenumber range of 4000-350 cm^{-1}, with 100 scans and 4 cm^{-1} resolution. All the samples were placed under the beam without any prior modification.

A.2.3 Transmission Electron Microscopy

Transmission electron microscopy (TEM) on the nanoparticles was performed using a Hitachi H9000 microscope, working at 300 kV. Scanning Transmission Electron Microscopy - High Angle Annular Dark Field (STEM-HAADF) images were obtained in a probe-corrected Titan (FEI) at a working voltage of 300 kV, coupled with a HAADF detector (Fischione). Samples for TEM observations of the nanoparticles dispersed in the ferrofluids were prepared by dip coating of carbon coated copper grids.

A.2.4 Cell culture and studies on cells

Prostate cancer cells (PC-3) were routinely cultured in RPMI-1640 medium supplemented with 10% FBS and 1% antibiotic/antimycotic. PC-3 cells were grown in cell culture treated t-15 flasks in a temperature-controlled incubator at 37 °, 5% CO_2 and in a humidified atmosphere. Upon reaching confluency cells were detached by using TripLE^{TM}Xpress and subcultured. μ-slide angiogenesis Ibidi imaging chambers (Ibidi GmBH, Germany), were coated with a nanoparticle suspension until a uniform layer was formed. Subsequently, Matrigel^{TM} was deposited on top of the nanoparticle layer and allowed to crosslink at 37 °C for 2h. This dual deposition strategy allowed for the formation of a cell adhesive substrate for PC-3 cells proliferation. Prostate cancer cells were then seeded at a density of 1:3 $\times 10^5$ cells/cm^2 and allowed to proliferate during 24 h. Irradiation was performed using a 850 NIR Led (Oslon PowerStar) with a power density 228 and 570 mW/cm^2 (according to specifications) during 5 min. The Fe3Se4 nanoplatelets on the wells were magnetized (set in a high state) using a cylindrical neodymium-iron-boron magnet (diameter 8 mm, height 30

mm, N42). The state before and after the irradiation procedures were measured using a F fluxgate magnetometer (FL1-100 Stefan Mayer Instruments) embedded in a permalloy foil to decrease the ambient magnetic field and noise at the fluxgate. On the following day cells were incubated with Calcein-AM/PI for 30 min at 37 °C. The cells were then washed 3 times with PBS and imaged.

A.2.5 Fluorescence Miscrocopy

Cells were then washed 3 times with PBS and imaged in a Zeiss Imager M2 fluorescence microscope (Carl Zeiss Microscopy GmbH, Germany), equipped with a 10x/0.25 air objective. All the data was processed in the Zeiss Zen software (Carl Zeiss Microscopy GmbH, Germany).

A.2.6 Magnetic data

Magnetic measurements were performed in a superconducting quantum interference device (SQUID) magnetometeres model MPMS-XL and MPMS3, from Quantum Design Inc, under helium atmosphere.

A.2.7 Magnetis Resonance Imaging

The ^{1}H NMR technique was used to measure the longitudinal and transverse relaxivities in a wide range of frequencies covering most of the clinical imagers ($\mu \approx 8.5$, 21, and 63 MHz correspondingto about 0.2, 0.5, and 1.5 T, respectively). For ≤ 10 kHz $\mu \leq 10$ MHz, the NMR data were collected with a Smartracer Stelar relaxometer (Stelar, Mede, Italy) using the Fast-Field-Cycling technique, while for n > 10 MHz a Stelar Spinmaster and an Apollo-Tecmag spectrometers have been used (Tecmag, Houston, TX). Standard radio-frequency excitation sequences Carr-Purcell-Meiboom-Gill-like and saturation recovery were applied to deter-mine T_2 and T_1 values.